NASA-CR-202393

FINAL TECHNICAL REPORT ON NASA NAGW-3408

PROTOPLANETARY FORMATION AND THE FU ORIONIS OUTBURST

Principal Investigator: P. H. Bodenheimer
University of California, Santa Cruz

The following three publications which reference the above grant from the NASA Origins of Solar Systems program are attached and form the final technical report for this project. The research involved comparisons of the spectral energy distributions of FU Orionis objects with theoretical models and associated studies of the structure of the outbursting accretion disks, as well as related studies on the effects of magnetic fields in disks, which will lead in the future to models of FU Orionis outbursts which include the effects of magnetic fields. The end date of the grant was 28 Feb 1995 with a no-cost extension to 28 Feb 1996. The project was renewed under a new grant NAGW-4456, entitled "Effects of FU Orionis Outbursts on Protoplanetary Disks". Work now being prepared for publication deals more specifically with the issue of the effects of the outbursts on protoplanetary formation.

Models of the spectral energy distribution of FU Orionis stars. Turner, N., Bodenheimer, P., and Bell, K. R. 1996. ApJ, submitted

A simple model of a buoyant magnetic dynamo in accretion disks. Rozyczka, M, Turner, N., and Bodenheimer, P. 1995, M.N.R.A.S. 276, 1179-1184

A numerical study of magnetic buoyancy in an accretion disk. Rozyczka, M., Bodenheimer, P., and Lin, D. N. C. 1996. ApJ, 459, 371

Models of the Spectral Energy Distributions of FU Orionis Stars[1]

N. J. J. Turner, P. Bodenheimer
University of California Observatories/Lick Observatory and Board of Studies in Astronomy & Astrophysics, University of California, Santa Cruz, CA 95064, U. S. A.

and

K. R. Bell
NASA Ames Research Center, MS 245-3, Moffett Field, CA 94035, U. S. A.

ABSTRACT

Observed spectral energy distributions (SEDs) of FU Orionis, V1057 Cygni, and V1515 Cygni are fit by theoretical spectra, which are calculated from models consisting of outbursting accretion disks together with flattened envelopes. Temperature in the envelopes is determined by approximate radiative equilibrium with a central source. The disk models are two-dimensional and include reprocessing of disk radiation by the disk. The theoretical spectra are calculated using a radiative transfer code and frequency-dependent opacities, at a spectral resolution of $\lambda/\Delta\lambda = 14$. Excellent matches to the data are obtained for all three objects with reasonable model parameters. Radiative transfer is also used to calculate a time series of images showing the progress of an outburst as imaged through a B-band filter.

Subject headings: accretion disks: protostellar — stars: pre–main-sequence — stars: FU Orionis — stars: V1057 Cygni — stars: V1515 Cygni

1. Introduction

The FU Orionis phenomenon (reviewed by Herbig 1966, 1977; Hartmann, Kenyon & Hartigan 1993) represents a key event in the early history of a star which should provide us with important clues on the nature of pre-main-sequence stellar evolution and the formation of planetary systems. The three objects considered here are FU Orionis, which brightened by 6 magnitudes in 120 days in 1936–7, V1057 Cygni, which brightened by 5.5 magnitudes in 250 days in 1969, and V1515 Cygni, which showed a much longer rise time of about 20 years, reaching a peak about 1970. At present the three objects are respectively 1 mag, 3 mag, and 0.5 mag fainter than at maximum light. A recent observational summary is provided by Bell *et al.* (1995), henceforth referred to as BLHK.

---

[1]UCO/Lick Observatory Bulletin No. ...

The most likely explanation for the observed outbursts is rapid mass accretion onto the surface of a star, triggered by a thermal instability in the inner, ionized regions of a surrounding accretion disk (Paczynski 1976; Hartmann & Kenyon 1985; Lin & Papaloizou 1985). The principal physical effect that induces the instability is a heating rate, say by viscous dissipation, that increases more rapidly with temperature than does the cooling rate by radiative and convective transfer. This situation is likely to occur in the region of partial ionization of hydrogen where the opacity is a strongly increasing function of temperature. The details of the mechanism remain to be clarified, since current models rely on an arbitrary viscous dissipation parameter (α) and in some cases an arbitrary external perturbation. Objections have been raised, on observational grounds, to the disk model (Herbig 1989; Petrov & Herbig 1992), but by now it is clear that steady-state disk models can explain a number of the observed features (Hartmann & Kenyon 1985; Adams, Lada, & Shu 1987; Kenyon, Hartmann, & Hewett 1988; Kenyon & Hartmann 1989, 1991; Calvet, Hartmann, & Kenyon 1993; Hartmann, Kenyon, & Hartigan 1993). Moreover, certain features which are still difficult to explain with a model involving a disk with constant mass flux can be explained by the use of more elaborate, time-dependent, vertically resolved models (Kawazoe & Mineshige 1993; Bell & Lin 1994; BLHK).

The detailed models of BLHK, which take into account the radial and vertical structure of the disk as a function of time through a series of outbursts, form the basis of the present paper. The general picture is that the star-disk system is still at a sufficiently early stage of its evolution so that matter is falling onto the outer part of the disk from the surrounding interstellar cloud (Kenyon & Hartmann 1991) at a rate $\dot{M}_{in}$. The results of the calculations show that as long as $\dot{M}_{in}$ exceeds 5×10^{-7} $M_\odot$ yr^{-1} , independent of the viscosity parameter α, the thermal ionization instability is initiated only a few stellar radii out from the star, and the disk goes into outburst. The ionization front then propagates radially through the disk on a time scale a few times longer than the local thermal value, reaching a maximum radius not larger than 0.25 AU (Bell & Lin 1994). The duration of the outburst is determined by the local viscous diffusion time in the hot, ionized region. Once this region has been sufficiently depleted by accretion onto the central star, it cools, hydrogen recombines, and the outburst declines. The interval between outbursts is determined by $\dot{M}_{in}$, which controls the rate at which mass is added to the inner disk. Once the mass there has increased to the point where the temperature once again becomes high enough to ionize hydrogen, the outburst cycle repeats. Spontaneous outbursts by this mechanism can explain the light curve of V1515 Cyg, but to explain the more rapid rise times of FU Ori and V1057 Cyg a small density perturbation in the inner disk is required to initiate the instability. This general explanation has been used by Lin *et al.* (1994) to conclude that in the case of HL Tau the value of $\dot{M}_{in}$ is much larger than the accretion luminosity implied from the properties of the inner disk, so the object could be in the quiescent stage between outbursts.

The work of BLHK emphasizes comparison of models with observed light curves. In this paper we make further tests of the viability of the detailed two-dimensional models by comparing them with observed spectral energy distributions and photometric properties. Previous work

on comparison of disk models of the overall spectral energy distribution (Adams *et al.* 1987; Kenyon *et al.* 1988; Kenyon & Hartmann 1991; BLHK) have assumed that at each radius the theoretical disk radiates either the same spectrum as a black body at the disk surface temperature, or as a stellar photosphere at the same effective temperature. A different approach is followed here. Frequency-dependent radiative transfer models are obtained from the two-dimensional disk structures (§ 2). Reprocessing of light from the hot inner disk by the cooler outer disk surface is included. Theoretical spectra are obtained as a function of the angle of inclination between the rotation axis and the line of sight (§ 3) and the differences between spectra that include reprocessing and those that don't are emphasized. The results are compared in detail (§ 4) with observations of the spectral energy distributions of the three objects in the wavelength range 0.3–100 μm. The frequency-dependent information is then used to provide a detailed calculation of the light distribution as a function of position and time for the model that fits the light curve of V1515 Cyg. The implications of the results are discussed in § 5.

2. Numerical Disk models

In this section, we describe the disk models used to investigate the appearance of FU Orionis systems. The first component, outlined in § 2.1, is a one-dimensional, radial time-dependent set of disk evolution equations with parameters chosen in BLHK to produce an outburst with B light curves close to those observed in one of the three program objects FU Orionis, V1515 Cygni, and V1057 Cygni. A particular epoch of interest is then selected from the solution to the time-dependent equations, and the model is expanded (§ 2.2) into a set of vertical structure models at a sufficient number of radii to define $T(r, z)$ and $\rho(r, z)$, where r is the cylindrical radius and z is height above the midplane. Reprocessing caused by the illumination of one part of the disk surface by another is found to significantly raise surface temperatures at some radii. Our method for calculating this reprocessing is described in § 2.3. When the disk is quiescent and its luminosity is low, the central star may make an important contribution (§ 2.4). Finally in § 2.5, we add an envelope to account for the observed flat spectrum at long wavelengths. The resulting model disk, consisting of the vertical models modified by reprocessing, plus an envelope and central star, is shown schematically in Figure 1. From this structure, the spectra presented in § 4 are calculated as discussed in § 3.

2.1. Time Dependent Models

The outbursting disk is evolved through time by a numerical integration of a set of equations which represent the radial diffusion of disk material by viscosity. The equations are described in detail by Bell & Lin (1994) and consist of mass continuity, energy balance, and the ϕ component of the equation of motion (Bell & Lin, eqns 3-5). The energy equation includes viscous heating from a Shakura & Sunyaev (1973) α viscosity, radiative losses from the surface, radial diffusion of

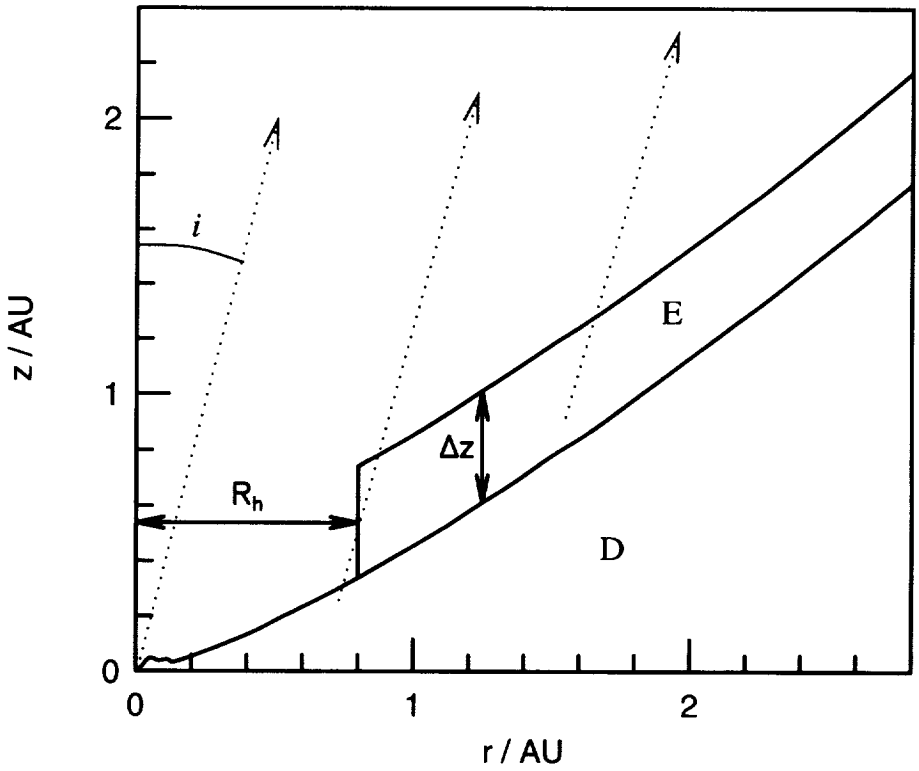

Fig. 1.— Model FU Orionis objects consist of a disk D and an envelope E. The envelope has a thickness Δz and a central hole of radius R_h. The object is viewed at an angle i from pole-on. The central star is located at the lower left. Also shown are three example lines-of-sight along which radiative transfer is carried out.

radiation, and $P\,dV$ work. In the region of outburst, the disk is not necessarily in vertical thermal balance. The opacity used in this initial stage is the analytic approximation to the Rosseland mean opacity described in the Appendix of Bell & Lin (1994). The values of α are the same as those used by BLHK: 10^{-4} throughout most of the disk where hydrogen is neutral, and 10^{-3} in regions where the hydrogen is ionized.

BLHK found that the observed light curves of the three objects were fit acceptably over a range of model parameters; these parameters include $\dot{M}_{in}$, and the size and type of density perturbation to the inner disk. In this paper we choose their models A1, B1, and C1 from which to calculate detailed spectral energy distributions; the models' parameters are listed in Table 1. Outburst in the B1 disk is spontaneous, but in A1 and C1 a small perturbation is required in order to match the rapid rise times of the FU Ori and V1057 Cyg outbursts. Such a perturbation might be provided in a clustered star-forming environment by interactions with nearby protostars. All three program objects lie in associations of young stars (see §3.4). Alternatively, the perturbations might be caused by radial migration of protoplanets (Syer & Clarke 1996) or by time variation of the effective viscosity in the outer disk. The perturbations are annuli of material added to the radial time-dependent models during the quiescent phase between outbursts. They have inner radii r_p, masses M_p, and a fractional surface density change within the annulus of $\Delta\Sigma/\Sigma$. Outer radii are determined by M_p and $\Delta\Sigma/\Sigma$.

2.2. Vertical Structure Models

In this subsection we discuss the sets of vertical structure models used to calculate spectra and images of the disk. The models provide the detailed distributions of temperature and density throughout the disk, $T(r,z)$ and $\rho(r,z)$. The vertical structure procedure is described in detail in Bell & Lin (1994); the essence of the program and several modifications are described here and in § 2.3. The basic procedure is as follows:

1. Start by calculating a set of vertical structure models, for example, for model C1 of BLHK.

Table 1: Disk outburst model parameters

Star	Model	$\dot{M}_{in}$ $M_\odot$/yr	M_p / $M_\odot$	$\Delta\Sigma/\Sigma$	r_p/ $r_\odot$
FU Orionis	A1	3×10^{-6}	0.01	5	13
V1515 Cygni	B1	1×10^{-5}	0	0	—
V1057 Cygni	C1	1×10^{-6}	0.002	3	10

Note: Table 2 in Bell *et al.* 1995 (BLHK) contains two misprints, which are corrected here.

2. Use the resulting disk surface properties, $T_e(r)$ and $H(r)$, to calculate the flux of energy deposited at a given point by illumination from other points of the disk.

3. Add this flux at the level where Rosseland optical depth $\overline{\tau} = 2/3$ to get a new effective temperature at each radius.

4. Calculate a new set of vertical structure models with this new boundary condition.

In the remainder of this subsection we discuss the first of these steps. The remaining three points are discussed in § 2.3.

The radial solution provides the disk effective surface temperature T_e and degree of departure from vertical thermal balance, at each radius. Calculation of the vertical structure model begins near the surface of the disk. Surface pressure is chosen so as to balance the weight of the overlying atmosphere, which is otherwise ignored. In the vertical models calculated before reprocessing, the boundary lies at $\overline{\tau} = 2/3$, while in the final vertical models from which spectra are computed (§ 2.3), it lies at $\overline{\tau} = 0.03$. Pressure and flux are next integrated towards the disk midplane. The pressure gradient balances the exact expression for the gravitational attraction of a central point mass – that is, finite disk thickness $H \approx r$ is allowed. The flux gradient includes terms due to local energy generation by viscous dissipation, and transport by both mixing-length-theory convection and radiative diffusion. Diffusion in the optically thin surface layer (and throughout the vertical model) is flux limited as in Bodenheimer *et al.* (1990), and scattering is assumed to be negligible. The opacity is the same approximation to the Rosseland mean as used by Bell & Lin (1994), although the final vertical models use the more complete opacities discussed in § 2.3. Finally, the disk height is adjusted and the integration is repeated until it yields zero flux at the midplane.

Vertical structure models are calculated at 190 values of the radius, evenly-spaced in $\log r$ from $r = 3R_\odot$ to $r = 158$ AU. Time dependent models provide radial points out to $100R_\odot \approx 0.5$ AU. Beyond this, the disk is assumed to be transporting mass in vertical thermal balance at the rate $\dot{M}_{in}$. Vertical models each consist of 100 points, with a grid adaptively-spaced so as to resolve steep z gradients in temperature occurring near the surface: the gap between points is held to no more than one twentieth of the local temperature scale height $T/(\partial T/\partial z)$.

2.3. Reprocessing

During outbursts, models' luminosities may exceed 100 $L_\odot$, most of which is emitted by the portion of the disk inside 0.25 AU (the "inner disk"). Some fraction of the photons emitted by the inner disk is intercepted by the outer disk, heating it significantly. While the inner disk has a spectrum peaking in the visible, the outer disk is heated to temperatures such that its peak flux is at wavelengths $\lambda \geq 2$ μm. The additional flux proves useful in matching the observed fluxes at wavelengths 2–5 μm (§ 4.1). The effect of this "reprocessing" has been studied in the limit of a thin disk with central star by Adams & Shu (1986). In comparison, a disk whose surface is concave

up, or flared, occupies a larger solid angle as viewed from the central source, and intercepts a larger fraction of the photons (Kenyon & Hartmann 1987; Ruden & Pollack 1991). All of these calculations, however, approximate the central source by a sphere of uniform temperature.

The construction of a pseudo-two-dimensional disk, described in the previous two subsections, results in a disk surface with several local maxima as shown in Figure 2. In calculating the temperature distribution arising from reprocessing in this case, one must consider how the wrinkles hide the bright inner disk from some regions of the outer disk. The details of the numerical procedure developed to handle this problem will be discussed by Bell (1997). The calculation assumes that the disk is solid at the $\overline{\tau} = 2/3$ surface, and radiates and absorbs like a black body. The calculation is done for the entire disk, not accounting for the presence of an envelope. The disk surface is divided into concentric rings by cylindrical radius ω, and the rings are subdivided by equatorial angle ϕ into surface elements. To calculate the reprocessing at a point $(\omega_0, \phi = 0)$ on the disk surface, a line of sight is drawn to each other point (ω, ϕ). Normals to the surface at the two points are projected onto the line of sight between them. If the components are directed towards one another, there is possible mutual heating. Finally, the line of sight is traced to determine whether an intervening fold of the disk obscures the end points from one another. The sum F_{in} of the fluxes arriving from all emitting points determines the reprocessing temperature T_{rp} at the point $(\omega_0, 0)$, in balance with losses by black body radiation, via

$$\sigma T_{rp}^4 = F_{in}. \tag{1}$$

The revised effective temperature at $(\omega_0, 0)$ is then

$$T_{e,tot} = (T_e^4 + T_{rp}^4)^{1/4}. \tag{2}$$

New vertical structure models are next computed starting from the revised effective temperatures. Since the surface layer will be important in the radiative transfer calculation, the vertical structure calculation is now begun at an optical depth of $\overline{\tau}_0 = 0.03$. The temperature at this new starting point, T_0, is found from the effective temperature using the Eddington approximation, $T_0^4 = \frac{3}{4} T_{e,tot}^4 (\overline{\tau_0} + 2/3)$. If the resulting T_0 is less than the reprocessing temperature T_{rp}, it is set equal to T_{rp}. This approximately represents the deposition of energy into the disk atmosphere by reprocessing (calculated in detail by Calvet *et al.* 1991), which was ignored in the calculation of lines-of-sight across the $\overline{\tau} = 2/3$ surface. Because the flux to be reprocessed enters the disk from both above and below, the net flux through the disk surface is unchanged when reprocessing is included and in vertical thermal balance is still equal to the flux due to viscous energy generation. Thus the surface flux used in the calculation of the new vertical structure is still σT_e^4.

The Rosseland mean opacities used in the new vertical structure models were provided by Alexander (1995); they correspond to the frequency-dependent opacities described in § 3.1 and used in the radiative transfer calculation of § 3.2. At temperatures and densities outside the table calculated by Alexander (1995), the Rosseland mean opacities of Pollack *et al.* (1985)

(low temperatures), Alexander, Auguson, & Johnson (1989) (higher temperatures), and Cox & Tabor (1976) (any remaining points) are used.

Temperature profiles for the B1 model with and without reprocessing are shown in Figure 3. Without reprocessing, the temperature outside the outburst region varies as $r^{-3/4}$, as in standard constant mass-flux accretion disk models. With reprocessing, there is a slight enhancement in temperature in the outburst region, inside the radius where the disk reaches a local maximum in thickness. Here, opposite sides of the disk are tilted towards one another across the central axis. We refer to this region as the "volcano". The most important effect of reprocessing, however, occurs at radii 0.1–10 AU, wherever the disk scale height is large enough so the surface sees over the near rim of the volcano to the hot region within. Because the reprocessing is set by the run of disk scale height with radius, and the scale height increases with opacity (Bell *et al.* 1997), the inner edge of this reprocessing region lies near the minimum in the disk thickness, which corresponds to the radius where the temperature is just low enough for dust grains to condense. In the spectra calculated in § 4.1, only the inner edge of the reprocessing region plays a rôle. The rest is hidden beneath an envelope. However, the radiative equilibrium approximation used in the envelope (§ 2.5) yields a temperature nearly continuous with that of the disk beneath, which was calculated by reprocessing for the disk alone. The match indicates that the disk surface temperatures are also approximately correct for the case where the disk is covered by the envelope. Because the envelope is optically thick, the surface temperature of the disk beneath the envelope plays no part in determining the SED.

Over the range of radii where reprocessing is important, the disk's temperature profile is flattened almost to $T \sim r^{-1/2}$. As one moves from the inner edge of this range to the outer, the disk height increases faster than the radius, the surface turns concave away from the midplane or "flared", and an increasing fraction of the inside of the volcano is visible from the disk surface. Beyond $r \approx 10$ AU, reprocessing is insignificant because the disk surface is concave towards the midplane and the bright inner disk is hidden from view. This change in curvature is due mostly to the opacity law $\overline{\kappa}(T)$ (Bell *et al.* 1997). Below the water ice condensation temperature of 125 K to which the disk material falls near 10 AU, $\overline{\kappa}$ is proportional to T^2, while in warmer material the opacity varies more slowly with temperature.

The main change in the disk's vertical structure due to inclusion of reprocessing, apart from the rise in surface temperature, is an increase in the thickness of the surface layer. The increase is greatest at radii between 4 and 8 AU, where reprocessing thickens the disk by 10%. At the midplane, temperature and density nowhere change more than 1.6%. For this reason, the extra energy input from reprocessing is not expected to significantly change the time evolution of the radial disk model. The calculation of reprocessing and resulting new vertical structure models can in principle be iterated until the disk thickness and effective temperatures both converge. However, we limit our procedure to one pass because experimentation has shown that the bulk of the effect is achieved after a single application. As discussed above, the inner 0.1 AU, where almost all of F_{in} originates, is altered only slightly by the reprocessing calculation.

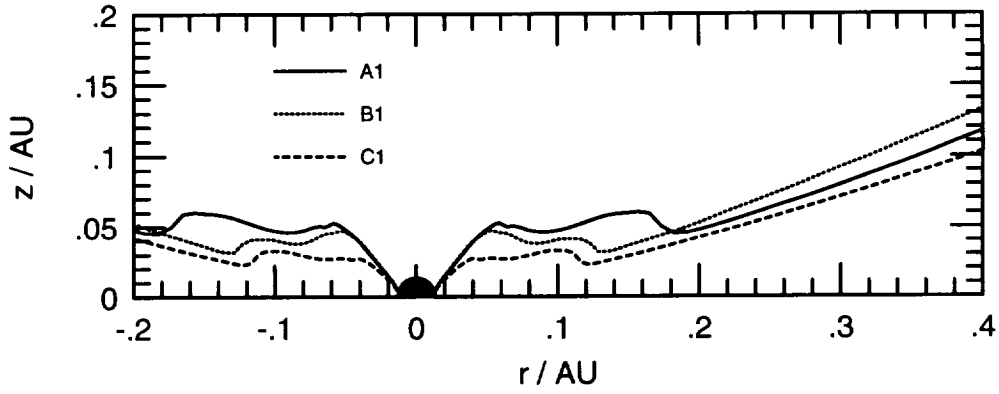

Fig. 2.— Shapes of the $\tau = 0.03$ surfaces of the inner, outbursting parts of the three disk models, showing the hot "volcanos" surrounding the central star (black dot). Scales on the horizontal and vertical axes are the same, so the disks are shown in their true proportions and the extent of reprocessing can be gauged.

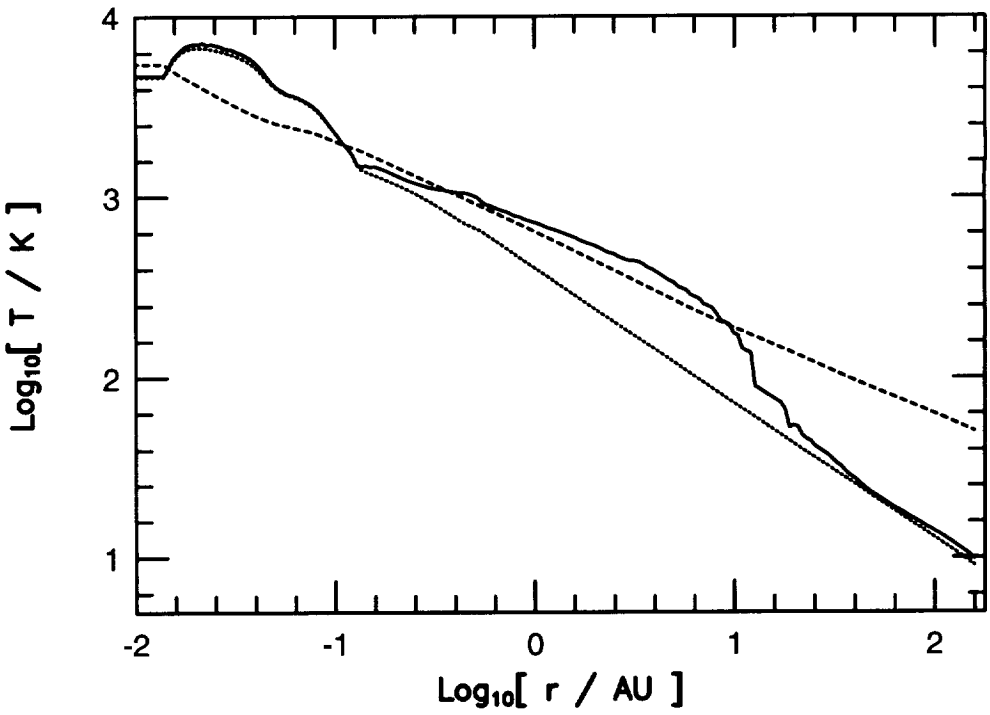

Fig. 3.— Disk temperature at the $\tau = 0.03$ surface versus radius in the B1 model, with reprocessing (solid line) and without (dots). Also shown is the temperature at the base of the envelope for each radius (dashes).

2.4. Central Star

Since the innermost radius r included in the disk models is $3R_\odot$, we must choose temperature and density distributions for $r < 3R_\odot$. If the central star is a T Tauri star of Solar mass and luminosity, its surface temperature and radius are between 3 000 and 4 000 K and about $3R_\odot$, respectively, implying that during outburst, the star's own luminosity is negligible compared with that of the inner disk. However, the structure of the region where the disk meets the star is not known. Does the disk engulf the star with hotter material in outburst, as suggested by the two-dimensional radiation hydrodynamic calculations of Kley & Lin (1996)? The disk model does not account accurately for the interface between disk and star. It assumes Keplerian rotation even at $r = 3R_\odot$, whereas at this radius the radial pressure gradient is large, suggesting some departure from Keplerian rotation. At $r = 3R_\odot$, the model disks' half-thicknesses are about $1R_\odot$.

As a test of the importance of the innermost $3R_\odot$ to the integrated spectrum during outburst, two spectra were calculated as described in § 3.2. For the first, the central $3R_\odot$ was occupied by a sphere of uniform surface temperature 3 400 K. For the second, the vertical structure of the disk model at $3R_\odot$ was copied to smaller radii. The models' effective temperatures at $3R_\odot$ are 5–6 000 K, while their midplane temperatures are 1.0–1.2 $\times$ 10^5 K. The resulting spectra differ by at most 0.016 decade in flux over the entire wavelength range. In the remainder of this paper, the center of the disk is occupied by a star of temperature 3 400 K and radius $3R_\odot$.

2.5. Envelope

FU Orionis stars show flux excesses at infra-red wavelengths $\lambda \gtrsim 10$ μm when compared both with normal giant stars and with equilibrium dusty disks. In V1057 Cygni, the excess diminished after outburst in step with flux at B-band, suggesting the 10 μm flux may be due to absorption and re-emission of radiation from near the central object by material out of the plane of the disk, such as a circumstellar envelope (Kenyon & Hartmann 1991). As we have seen in § 2.3, the excess cannot be fully explained by disk reprocessing, because reprocessing does not heat the disk surface outside about 10 AU radius. For a viewer on the surface outside this radius, the outburst region is hidden by the curve of the disk.

Our simplified model of the envelope is a layer of uniform thickness, touching the top of the disk, and with a central hole exposing the inner disk (Figure 1). This structure for the envelope is suggested by the results of two-dimensional collapse calculations, in which the density structure of matter infalling onto a disk is closer to plane-parallel than to spherical geometry, and most of the optical thickness is just above the surface of the disk (Yorke, Bodenheimer, & Laughlin 1993). Our envelope is made from material with the same opacity function as that in the disk (§ 3.1). The temperature T_d in the envelope a distance d from the center of the system is calculated assuming the envelope dust is in approximate radiative equilibrium with the object's hot inner region. That is, the rate of energy loss by radiation is balanced by the rate at which radiation from the hot

region falls on the dust:

$$4\pi\sigma T_d^4 = \frac{L_{il}}{4d^2}, \tag{3}$$

where L_{il} is the "illumination luminosity", the portion of the luminosity of the outbursting part of the disk which is intercepted by the envelope. This temperature distribution is correct for an optically thin medium. For an optically thick medium, equation (3) is also approximately correct. This is indicated by the radiative transfer calculations of Hartmann, Kenyon & Calvet (1993) for spherical optically thick envelopes around Herbig Ae/Be stars, and of Kenyon, Calvet & Hartmann (1993) for spherically symmetric protostellar envelopes in which density is proportional to $d^{-3/2}$. The variations of temperature with distance resulting from these calculations range from $T \sim d^{-0.75}$ to $T \sim d^{-0.4}$. In non-spherically-symmetric models Yorke *et al.* (1993) find $T \sim d^{-1/2}$ also, in both optically thick and optically thin regions. For a thin disk, $T \sim d^{-1/2}$ reduces to $T \sim r^{-1/2}$, which yields a flat λF_λ spectrum (Adams, Lada & Shu 1988) as observed in FU Orionis objects at $\lambda \gtrsim 5$ μm.

The parameters which fix the geometry of the envelope are its thickness Δz parallel to the disk axis, the radius of the central hole R_h, and the extinction A_V^{ENV} through the thickness. At the inner edge of the envelope, Δz is larger than the disk thickness. Density in the envelope is chosen so as to yield the specified extinction at temperatures between 125 K and 800 K. Opacities in this temperature regime are described in § 3.1. The thickness of the disk beneath the envelope is determined including reprocessing, but because the disk thickness is changed at most 10% by reprocessing, the effect on the spectrum is negligible.

When the optical depth through the envelope is less than unity, the spectrum of the envelope appears as emission or absorption lines superposed on the spectrum of the disk. These lines, due to water ice and silicates, appear at wavelengths 3–30 μm. Such lines do not appear in spectra of FU Orionis and V1057 Cygni (Cohen 1980) (except during dimming events such as that experienced by V1057 Cygni in 1995 – Wooden *et al.* 1995; Wooden 1996). The lines are absent from the models' spectra provided that at each radius the envelope has an optical depth greater than unity at wavelengths where it and the disk beneath it contribute significantly to the integrated SED. When this condition holds, the spectrum is also insensitive to both the density in the envelope and its variation with radius. The condition is satisfied when the extinction through the envelope is uniformly above $A_V^{ENV} = 100$ magnitudes. It is satisfied almost everywhere when density varies as the inverse square root of the disk radius, with $A_V^{ENV} = 100$ magnitudes at disk radius $r = 1$ AU. Such a density distribution is obtained when a spherical $\rho \sim d^{-3/2}$ distribution is flattened vertically into a disk. The region where the condition is not satisfied in this case is outside 25 AU, where the envelope is now optically thin at wavelengths $\gtrsim 30$ μm. Compared with the case where the condition is satisfied throughout the envelope, this results in a spectrum which falls off more rapidly as λ increases past 30 μm. Throughout the remainder of this paper, density in the envelope is held uniform and equal to the value which results in $A_V^{ENV} = 100$ magnitudes. Resulting densities lie between 10^{-14} and 10^{-12} g cm^{-3}, for the parameters listed in Table 3. Corresponding mass infall rates can be estimated using the results of the calculations of Yorke *et*

al. (1993). Typical velocities perpendicular to the disk surface for the infalling material in their simulations are about 3 km s^{-1}. When the infalling material has a density of 10^{-14} g cm^{-3} over the inner 25 AU of the disk, this yields a mass infall rate of $10^{-5} M_\odot$ yr^{-1}, similar to the rates used in the time-dependent disk models (Table 1).

If the model FU Orionis objects were fully self-consistent, the envelope temperature as set by L_{il} would be continuous with the temperature of the disk hidden beneath it. However, as Figure 3 indicates, while the temperature calculated from reprocessing agrees quite well with the dust equilibrium temperature assigned at the same radius throughout most of the disk, there is significant departure outside $r = 10$ AU, where the curve of the disk hides the hot inner regions from points on the disk surface. Here we maintain illumination of the envelope since the radiation transfer calculations of Yorke *et al.* (1993) indicate that in the infalling material $T \sim r^{-1/2}$, independent of the optical depth along the line of sight to the central source.

3. Calculation of emergent radiation

3.1. Wavelength-dependent opacities

New opacities for use in the radiative transfer calculation were obtained from Alexander (1995), calculated as described in Alexander & Ferguson (1994) for the S92 composition (Seaton *et al.* 1994) with $X = 0.70$ and $Z = 0.02$. All known sources of opacity which are significant at temperatures between about 700 K and 12 500 K are included. Alexander convolved monochromatic opacities with a Gaussian filter of half-width equal to 2% of the inverse wavelength, because of the very broad range of wavelengths to be covered. The result is a table of opacities $\kappa_\lambda(R, T)$ averaged around 100 wavelengths λ. R is equal to $\rho/(T/10^6\ \mathrm{K})^3$. The 100 wavelengths are evenly spaced in $\log \lambda$ from 100 nm to 100 μm. Spectral resolution is thus $\lambda/\Delta\lambda = 14$, sufficient to reveal individual strong lines. For example, Hα at wavelength 656 nm is represented by one opacity value on the line, and adjacent continuum values. The table has entries every 0.5 decade in R and every 0.2 decade in T, except for temperatures from 800 K to 3300 K, which bracket rapid changes in opacity due to dust evaporation and ionization. Here there are entries every 0.1 decade in T. A few points required for the radiative transfer calculations fall outside the available R and T. In these cases, we use κ_λ at the same T and the nearest available R.

Below 700 K, there is only sparse data available on the optical properties of the materials which condense as dust grains, and the opacities are less reliable. In the absence of better frequency-dependent low-temperature opacities, Alexander's 800 K opacities are used in the present calculation down to a temperature of 125 K. These opacities include grains made of silicates, iron, amorphous carbon, and silicon carbide. Graphite is not included in the Alexander opacities, presumably because its importance in protostellar environments is controversial (Pollack *et al.* 1994). Yorke (1979) also provides opacities in this temperature range, but for silicate grains only. Neither Yorke's data, nor the extrapolated Alexander data has temperature or density

dependence. The Yorke values are slightly lower than the total opacities of Alexander at most wavelengths. For temperatures of 125 K and below, water ice becomes an important source of opacity. We use the sum of Yorke's (1979) opacities due to water ice and silicates.

3.2. Spectra

Radiation emerging from a distribution of density $\rho(r, z)$ and temperature $T(r, z)$ is calculated by integration of the equation of radiation transfer (Mihalas 1978)

$$\frac{dI_\lambda}{d\tau_\lambda} = I_\lambda - S_\lambda \tag{4}$$

along a set of lines of sight through the distribution. The numerical procedure is a modification of that described by Yorke (1986). The source function used is a black body, $S_\lambda = B_\lambda(T)$. The optical depth τ_λ is defined by $d\tau_\lambda = \kappa_\lambda \rho \, dx$, with wavelength-dependent opacity $\kappa_\lambda(\rho, T)$. Equation 4 is solved separately at each wavelength. Wavelengths used are those for which opacities are provided (§ 3.1). For a given line of sight, optical depth $\tau_\lambda = 10$ is located by integrating from the observer into the medium. The outward integration, which determines the emergent specific intensity, then begins at this point. The specific intensity I_λ is set equal to the black-body intensity B_λ corresponding to the local temperature, and equation 4 is integrated back towards the observer. At each integration step, the step length Δx is chosen so that its optical depth $\Delta\tau_\lambda = \kappa_\lambda \rho \Delta x$ is at most 0.1, and also so that it is shorter than one third of the local spatial resolution of the outburst model. If this step would leave or enter the material making up the disk or envelope, the step length is shortened so as to end the step within 10^{-5} $R_\odot$ of the boundary. This ensures physically thin layers have the correct optical depth, and abrupt opacity and temperature changes near boundaries are well-represented in the integration. As needed for finding the source function and opacity along the line of sight, density and temperature are linearly interpolated on the non-rectangular grid made by the series of vertical models. Opacity at each wavelength is found by interpolating in log space on the grid of densities and temperatures described in § 3.1.

The integrated spectrum of the model is calculated by summing emergent spectra over regular square grids of lines-of-sight. Because temperature variation in the disk occurs over small spatial scales near the star, and larger scales further away, a nested, concentric set of line-of-sight grids is used. The innermost grid is 0.2 AU across, and successive grids are five times wider. The outermost extends to 125 AU radius. When viewed from directly over the pole, the disk is circularly symmetric, and the grids are one-dimensional, each with 51 lines-of-sight along the radius. For inclination angles $0 < i < 90°$, the view of the disk is symmetric only about the plane containing the polar axis and the line-of-sight. In this case, each grid is two-dimensional, and consists of 51 lines-of-sight along the radius perpendicular to the symmetry axis and 101 along the diameter parallel to the symmetry axis. The resolution on the innermost grid is 0.004 AU, or $0.85 R_\odot$. With the disk models described here, increasing the resolution beyond this level produces negligible change in the total spectrum.

The apparent magnitude of the model in the B spectral band is calculated by integrating in wavelength the product of the spectrum F_λ and a filter transmission curve, and applying the calibration between integrated flux and magnitude of Colina & Bohlin (1994). The filter transmission curve used is that tabulated by Johnson (1965).

3.3. Images

The same radiative transfer calculation which yields the integrated spectrum of the object also yields a spatially-resolved image. Solution of the radiative transfer equation along a line of sight yields the spectrum of radiation emerging from the disk at one point. A flux is found by integrating in wavelength the product of this spectrum with a filter transmission curve. Fluxes from all the lines of sight are assembled on a grid, making an image of the object.

3.4. Distances and Extinctions

To match the absolute level of a physical model against that of an observed spectral energy distribution, we need the distance to the object and the amount of obscuring material along our line of sight. Measurements of these quantities for the three objects are collected in Table 2. The estimate of the distance to FU Orionis is taken from Murdin & Penston (1977), that of the distance to V1057 Cygni from Straizys *et al.* (1989). The distance to V1515 Cygni was estimated by Racine (1968). Extinctions to the three objects were assembled by BLHK. In adding extinction to the calculated spectra, we scale the wavelength dependence of interstellar absorption (Mathis 1990) so as to obtain the desired extinction at 0.55 μm, the central wavelength of the V band.

Also in Table 2 are the luminosities of the objects and the corresponding models. The quantities listed are apparent B magnitude; de-reddened B-band luminosity; and de-reddened total luminosity, integrated from 0.380 μm to 100 μm. B-band luminosities were calculated from the apparent magnitudes assuming $R_V = A_V/E(B-V) = 3.1$. Total luminosities were calculated by integrating the spectral energy distributions of Kenyon & Hartmann (1991), assuming for

Table 2: Distances, Extinctions, and Current-Epoch Luminosities of FU Orionis Objects

Star	Distance	A_V	B Mag		$L_B/L_{B,\odot}$		$L_{tot}/L_\odot$	
	pc	mag	Data	Model	Data	Model	Data	Model
FU Orionis	400 ± 60	2.0	10.6	10.64	160	160	250	260
V1057 Cygni	550 ± 100	3.1	13.4	13.79	90	50	250	200
V1515 Cygni	1000 ± 200	2.8	13.7	13.59	160	170	230	290

V1515 Cygni a falloff at long wavelength with the same shape as that of V1057 Cygni. The models' B-band and total luminosities were calculated using the methods of § 3.2 and the parameters of Table 3. The discrepancy between the luminosities of the C1 model and V1057 Cygni was resolved by placing the C1 model at 500 pc rather than at 550 pc (see § 4.1). This lies within the uncertainty in the distance measurement. The apparent B magnitude of V1515 Cygni was found by extrapolating the light curve through a dimming which began in 1980 (Kenyon *et al.* 1991). The B-band luminosity calculated for V1515 Cygni from the magnitude is thus not directly comparable with the total luminosity, which is calculated from a SED which includes the effects of the dimming.

4. Results

4.1. Spectral Fits

Figure 4 shows our best matches to recent observed spectral energy distributions of the three stars. These are the data collated by Kenyon & Hartmann (1991), but without de-reddening. SED points are placed at the nominal wavelengths of the photometric bands, which in most cases are effective wavelengths for equal input energy at all wavelengths. Filter transmission curves are taken from Johnson (1965) for bands *UBVRI* and N; from Bessell & Brett (1988) for *JHKLM*; and from references under Kenyon & Hartmann (1991) for other bands. The models' parameters are given in Table 3.

Figure 4 also shows that the B1 model spectrum coincides with the V1515 Cygni data at B-band, and is an excellent fit at other wavelengths, if it is reddened by $A_V = 3.2$ mag instead of the nominal $A_V = 2.8$ mag. Some of the V1515 Cygni data were obtained while that object had not fully recovered from a dimming it experienced beginning in 1980. The dimming, which is thought to be a dust condensation event, was accompanied by an increase in the object's reddening (Kenyon *et al.* 1991).

The data in Figure 4 include measurements obtained over about ten years, so a little caution is needed in matching them with models of any particular epoch. For example, points at 12, 25, 60, and 100 μm were obtained with the Infra-Red Astronomy Satellite (IRAS) in 1983-84, while near-infrared data were obtained by Kenyon & Hartmann in 1989-90. The spectra are calculated from models at epoch 1993.

4.2. Comparison with Other Spectral Fits

In this subsection we compare the fits generated in § 4.1 with those obtained in previous attempts to model the spectral energy distributions of FU Orionis stars using accretion disks.

The models of Adams *et al.* (1987) are constant mass-flux accretion disks, with excess IR emission arising in dusty shells, remnant wedges of the objects' spherically-symmetric parent molecular cloud cores lying $\geq 1 - 10$ AU from the central object. A spectrum, calculated assuming blackbody emission from the disk and envelope and grain opacities in the envelope, matches the spectrum of FU Orionis adequately at visible wavelengths, but rises from 10 to 30 μm, in conflict with the data presented in Kenyon & Hartmann (1991) and plotted in Figure 4.

The models of Kenyon, Hartmann & Hewett (1988) are also constant mass-flux accretion disks, but without a source of excess IR emission. Spectra are calculated by assigning each disk annulus the fluxes of a supergiant star of the same effective temperature, and summing over the disk. Annuli with temperatures below 3 500 K are assigned blackbody spectra. The resulting fits to FU Orionis and V1057 Cygni are adequate at wavelengths of 0.35–1 μm, but too bright by almost a magnitude at 2 μm, and too faint by over a magnitude at 20 μm.

In the flared-disk models of Kenyon & Hartmann (1991), a constant mass-flux disk reprocesses light from a central star. The surface of the disk is bent into a shape $H \sim r^{9/8}$, where H is the disk thickness and r is the cylindrical radius. This makes reprocessing more effective than in a flatter, standard constant mass-flux disk. Spectra are calculated as in Kenyon *et al.* (1988). The fluxes at 3–30 μm are higher than those from non-reprocessing disks, but in the wavelength region longward of 5 μm, which we match using a transition from disk to envelope, the best-fit flared-disk models of FU Orionis and V1057 Cygni are too bright at short wavelengths and too faint at long wavelengths. Kenyon & Hartmann (1991) also present spectra calculated from models of V1057 Cygni which include a spherically-symmetric dusty envelope and a steady accretion disk. The radial optical depth of the model envelopes at wavelengths 5–50 μm is close to unity. The spectra match the observations well, except that they show broad features at 3–30 μm which do not appear in higher-resolution observations of FU Orionis and V1057 Cygni (see § 2.5).

The SED fits in Figure 4 are more detailed in several ways than the three others just discussed. They are calculated from outbursting disk models in which the mass flux varies with radius; the models include reprocessing of disk emission by other parts of the disk; and the shape of the disk surface is consistent with the underlying accretion model. An envelope is included, based on results of hydrodynamic collapse simulations; and the SEDs are calculated from the models by radiative transfer with fairly complete frequency-dependent opacities. The more detailed

Table 3: Parameters used in calculating the simulated spectra shown in Figure 4.

Star	Model	Distance/pc	i	$L_{il}/L_\odot$	R_h/AU	Δz/AU
FU Orionis	A1	400	30°	11	0.8	0.8
V1057 Cygni	C1	500	0°	30	0.1	0.1
V1515 Cygni	B1	1000	0°	33	0.2	0.4

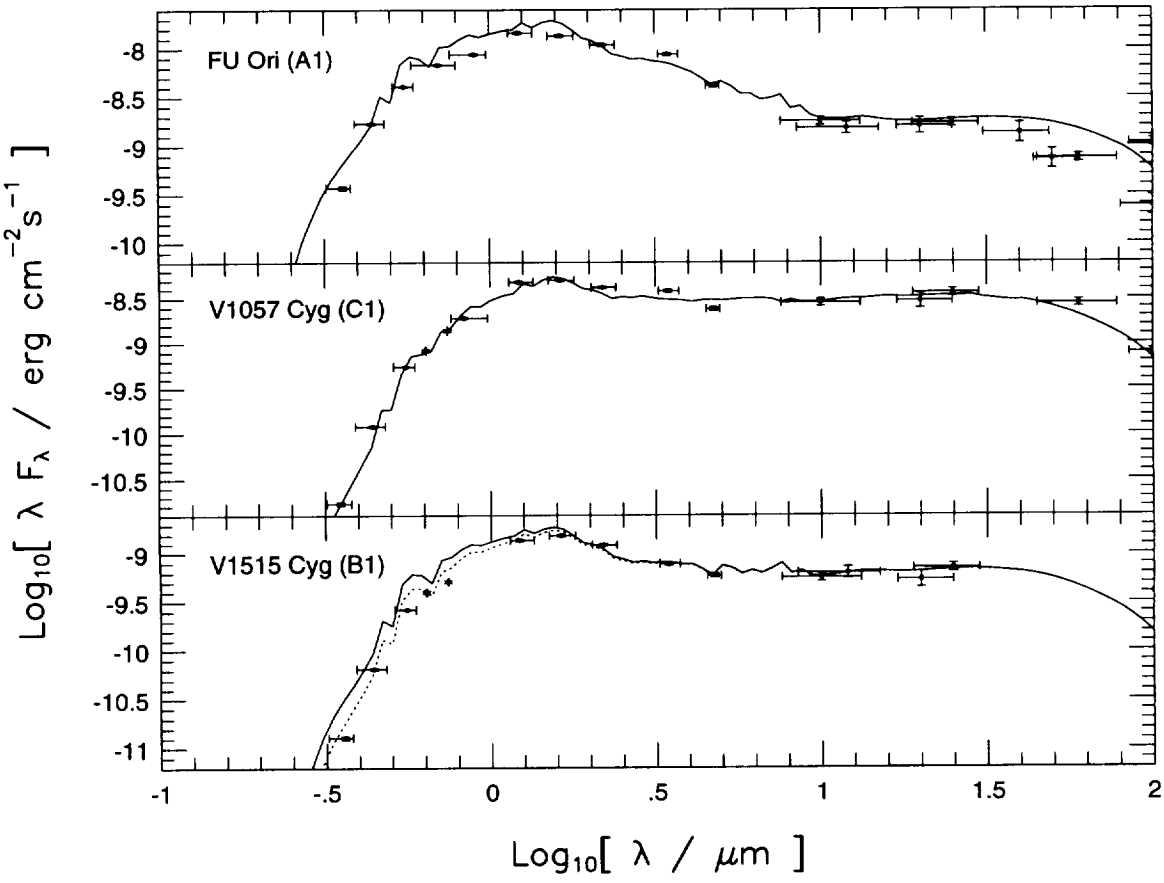

Fig. 4.— Fits (solid lines) to current-epoch un-dereddened observed fluxes from Kenyon & Hartmann (1991) (points), for the three objects. Vertical error bars on the data points show the quoted uncertainties in fluxes. Horizontal error bars extend to the wavelengths where filter transmission drops to 50% of its peak value. Where the wavelength range is short or the flux error is small, error bars lie inside the points. Interstellar reddening is included in the model spectra. The B1 model spectrum is also reddened an additional 0.4 mag (dotted line), as a possible way to allow for V1515 Cygni's sudden 1980 dimming. Parameters of the models are listed in Table 3.

calculation produces SEDs which match the observations closely, especially at wavelengths from 5 to 100 μm where the spectrum is determined largely by the envelope. The difference between observed and model fluxes is no more than about 0.25 mag at most wavelengths, with a few points off by up to 0.75 mag.

4.3. Parameter sensitivity

In the spectral fits of Figure 4, two sets of parameters vary the shape of the spectrum in two different wavelength regions. At visible and near-IR wavelengths, the flux is determined by the distribution of hot material, which is found only in the outbursting inner disk. At wavelengths longer than about 5 μm, the luminosity is dominated by large surface areas instead of high temperatures, and the flux is set by the envelope. At intermediate wavelengths, inner disk, reprocessing by the outer disk, and envelope can all be important, depending on the parameters. As discussed below, the parameter set needed to fit a spectrum is not necessarily unique.

The parameters which affect the disk portion of the spectral energy distribution are the viewing angle, i; whether reprocessing is included; the time-averaged mass flux $\dot{M}$ and mass of the central star, M_*, to both of which the disk luminosity is proportional; and the interstellar extinction, A_V. Parameters which influence the envelope part of the SED are the luminosity L_{il} of the outbursting disk as seen from the envelope; the envelope extinction A_V^{ENV}, thickness Δz, and central hole radius R_h; and the viewing angle i. Several of these parameters are restricted by data, while others are unimportant to the spectra. Among the disk spectrum parameters, M_* was set in the BLHK models to $1 M_\odot$ for all three objects. This is based on a pre-outburst spectrum of V1057 Cygni indicating it was a T Tauri star and hence roughly of Solar mass, and space density arguments which suggest FU Orionis objects cannot be precursors of high-mass stars (Herbig 1977). The mass fluxes were chosen by BLHK so the light curves of the model disks would match the observed time variation of B-band light (Table 1). Interstellar extinction is not treated as a parameter; we use the values discussed in § 3.4. The angle at which we view V1057 Cygni is restricted by rotational line broadening measurements to $i < 30°$ if the central mass is close to $1 M_\odot$, while the inclination of FU Orionis must be $25° < i < 70°$ (Kenyon *et al.* 1988). We choose to view the models pole-on ($i = 0°$), except for FU Orionis, for which we assume an inclination of 30°.

Among the envelope spectrum parameters, the extinction A_V^{ENV} is set to 100 magnitudes to ensure the envelope is optically thick at all wavelengths. Since the envelope has a temperature different from that of the underlying disk, an optically thin envelope would yield strong emission or absorption lines due to water ice and silicates at wavelengths 3–30 μm. These are not observed in FU Orionis nor in V1057 Cygni (Cohen 1980; Wooden 1996). Kenyon & Hartmann (1991) used an envelope extinction of 50 magnitudes. However, the inner parts of our envelope are too hot for ice grains to exist, and consequently have reduced opacity. For an envelope with $A_V^{ENV} = 50$ mag, where ice is solid the optical thickness is high, but wherever ice has sublimated

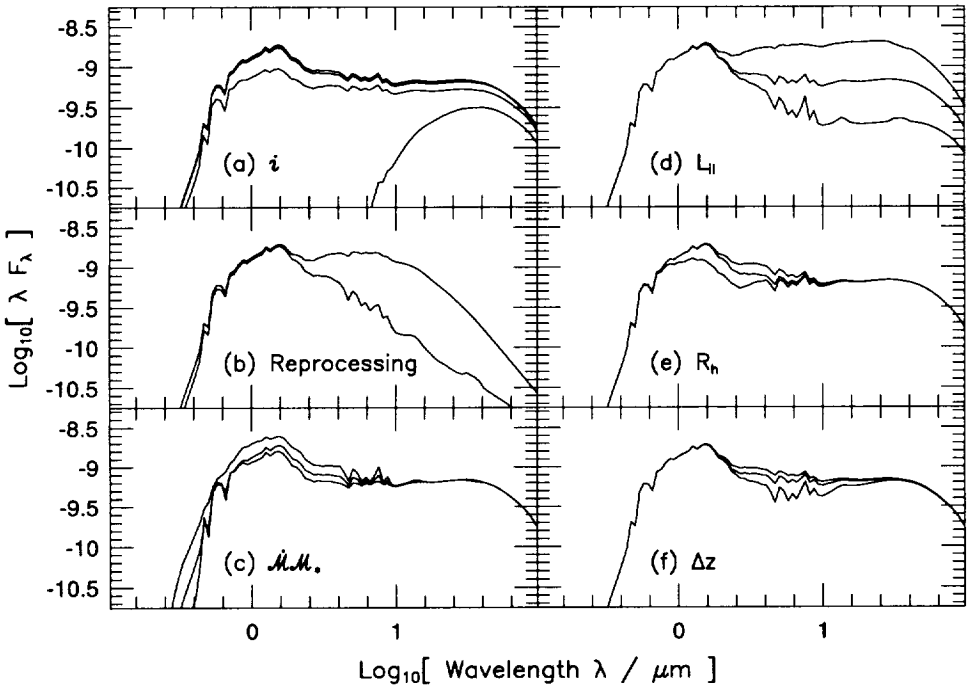

Fig. 5.— Sensitivity of the spectrum of the B1 model to three disk parameters (left) and three envelope parameters (right). The model is viewed (a) 0, 20, 40, and 60° from pole-on (top to bottom); (b) with (upper) and without (lower) disk reprocessing (the envelope has been removed); (c) with disk luminosity scaled up (top) and down (bottom) by factors of two; (d) with luminosity L_{il} illuminating the envelope scaled by factors of 3 (top) and 1/3 (bottom) from its best-fit value; (e) with the radius of the hole in the envelope varied likewise (a larger hole leads to a higher flux at 3 μm); (f) with the thickness of the envelope varied likewise (a thicker envelope leads to a lower flux at 3 μm). See § 4.3.

the optical thickness is less than unity at wavelengths $\lambda > 4$ μm. Increasing A_V^{ENV} beyond our chosen value of 100 mag has little effect on the spectra. Another envelope spectrum parameter, the luminosity L_{il} illuminating the envelope, is expected to be less than the total luminosity of the outburst region in the disk. Collapse calculations suggest that reasonable values for the envelope thickness Δz may lie in the range $0.1 - 10$ AU (Yorke *et al.* 1993). The hole radius R_h must be at least $5R_\odot$ if the hole is to expose the peak surface temperature in the outbursting disk, and must be $40R_\odot \approx 0.2$ AU if the entire outbursting region is to be visible.

Variation of the models' spectra over the remaining parameter space is illustrated in Figure 5, which sets out spectra calculated for the B1 model

(a) **at viewing angles i = 0, 20, 40, and 60°:** Increasing the viewing angle reduces the projected area of the disk, hence decreases the flux at all wavelengths. Beyond a critical angle, the inner edge of the envelope hides the central outbursting region, and the flux at visible wavelengths plummets.

(b) **with and without reprocessing:** The envelope is removed so the spectra reflect disk temperatures only. Reprocessing yields a spectrum which is almost flat at wavelengths of 3–10 μm, whereas a standard constant mass-flux accretion disk with $T \sim r^{-3/4}$ has a long-wavelength spectrum $\lambda F_\lambda \sim \lambda^{-4/3}$.

(c) **with values of $\dot{M}M_\star$ equal to one half, once, and twice the standard value:** The integrated disk luminosity is proportional to $\dot{M}M_\star$. To scale luminosity L, we scale temperatures throughout the disk as $L^{1/4}$ (Lin & Papaloizou 1985). Note that this scaling does not accurately represent changes in spectral lines. Since the envelope illuminating luminosity L_{il} is not adjusted, the spectrum is unaffected at wavelengths longer than a few μm.

(d) **with standard, one third, and triple luminosities illuminating the envelope:** The level of the flat spectrum is determined by the luminosity illuminating the envelope. A high L_{il} means a high starting temperature in the envelope's $T \sim r^{-1/2}$, and so a high flux at given wavelength.

(e) **with holes in the envelope of the standard radius, one third, and three times standard:** Increasing the radius of the hole exposes more of the disk material heated by reprocessing to temperatures of 1000–1500 K. Since the envelope at the same radius is cooler, exposing more of the disk raises the flux at 2–3 μm.

(f) **with envelopes of standard, one third, and triple thicknesses Δz:** Increasing the thickness of the envelope places the envelope's upper, visible surface further from the illuminating source. This reduces the flux from the envelope at wavelength 5 μm, and total flux at this wavelength falls to near that of the disk alone. In addition, unit optical depth in the thicker envelope spans a larger range of temperatures, resulting in stronger absorption lines which are not observed in these objects.

The mapping between models and spectra is not one-to-one. There exist combinations of the parameters for which the calculated spectra are almost identical. For example, changing the distance from which we view the model multiplies the spectrum by a factor independent of wavelength, shifting it vertically on our logarithmic plots. This is almost the same as the effect of changing the angle from which we view the model, provided the viewing angle is not so large that the hot central region of the disk is obscured. Changing the mass inflow rate $\dot{M}$, or equivalently the mass of the central star, M_*, scales the luminosity of the disk and so likewise shifts the continuous spectrum vertically. However, reasonable ranges in any of these parameters require only small changes in the accretion disk models. As the C1 model set up by BLHK is slightly less luminous than V1057 Cygni, we choose to place the model slightly closer than the star (§ 4.1). We could instead have increased its luminosity using the $M_*\dot{M}$ scaling described above under item (c). Since scaling luminosity scales the peak surface temperature of the disk, it moves the peak wavelength of the un-reddened spectrum. However, once several magnitudes of interstellar reddening are applied, the peak in the λF_λ plot always lies near the H-band, effective wavelength 1.63 μm, as fixed by the reddening curve.

The effects on the spectrum of the envelope hole radius R_h and thickness Δz are similar and small, and they occur in overlapping wavelength ranges. The hole radius would have almost no effect on the spectrum if our model envelope were fully consistent with the reprocessing applied to the model disk (§ 2.3), in which case the disk temperature and envelope temperature would be nearly continuous. Thus the precise assumed geometrical structure of the envelope is not critical. For good fits to the observed spectra, the important requirements on the envelope are (1) A_V^{ENV} must be large, and (2) the temperature distribution must be $r^{-1/2}$, as in equation (1).

The luminosity illuminating the envelope, L_{il}, is not degenerate with other parameters; the observed SEDs thus constrain the value of L_{il} for each object. The best-fit values listed in Table 3 are much less than the objects' total luminosities in Table 2. This occurs because equation (3) assumes isotropic radiation from the central region, whereas in fact the bulk of the total luminosity is emitted from deep inside the volcano, towards the pole, and plays no part in heating the envelope. Compared with the region inside the volcano, the portion of the inner disk which provides the chief illumination for the envelope has about twice the surface area and half the surface temperature (figures 2 and 3). Application of the Stefan-Boltzmann law thus suggests the envelope will be illuminated by a luminosity around one eighth that of the total for the object. According to Table 2 and Table 3, the envelope intercepts between one sixth and one twenty-fifth of the total energy emitted by the object.

More evidence that the disk models are compatible with the required L_{il} comes from close inspection of the disk surface shapes in Figure 2. The ratio of L_{il} (Table 3) to the total B-band luminosity of the object (which arises almost entirely in the outbursting region; Table 2) is highest for V1057 Cygni. The corresponding model, C1, has the smallest rim to its volcano, exposing hot material to the largest range of radii in the outer disk. The next-highest L_{il}/L_B is exhibited by V1515 Cygni (B1). Compared with FU Orionis (A1), its rim is smaller, its outer disk surface lies

higher, and its peak surface temperature occurs higher above the midplane. The three models' ranking in openness of their central volcanos is the same as the ranking of the objects in the relative luminosities L_{il}/L_B needed to explain the observed envelope spectra.

The models were truncated at a radius of 125 AU because the observed fluxes decrease with wavelength at $\lambda \gtrsim 50$ μm, corresponding to an envelope temperature of about 60 K. The disk surface temperature at the same radius is 10 K (Figure 3), comparable to that expected in the surrounding molecular cloud. The accretion disk model then breaks down because viscous heating is no longer the main energy input. Furthermore, radiative collapse calculations by Yorke *et al.* (1995) suggest that the disk plus envelope becomes optically thin near this radius. Thus the spectra would fall off beyond this wavelength even if the models were not truncated.

4.4. Simulated B-band images

Figure 6 shows the appearance of the inner 0.3 AU of the disk in the B1 model. This is the model whose spectrum and light curve match that of V1515 Cygni, but here its envelope is removed and it is viewed 30° from pole-on, through a B-band filter. Lighter areas of the images are brighter; the density of grey scales with the logarithm of the flux. The series of images is calculated from a series of B1 models spaced every 25 years through an outburst cycle. The series covers quiescence while material accumulates and slowly migrates in through the inner disk (1243, 1543, 1943), through onset, when the temperature at the inner edge of the disk rises high enough for hydrogen to be ionized, through the outward propagation of the ionization front (1968, 1993, 2093), and as the outburst declines (2168) and a new cycle begins (2193). Note the bright inner slope of the volcano, an asymmetric white crescent at the centers of the 1968, 1993, and 2093 images. Also, note the increased reprocessing in the outer disk during outburst. Reprocessing of illumination from a central star has been added to the disk models when they are quiescent. In outburst, the disk dominates total light. In quiescence, the disk is fainter than the star. The radius of the assumed star is $3R_\odot$, and its temperature is 3400 K. The images were computed as described in § 3.3. Though spatial scales this small in protostellar accretion disks are unlikely to be directly imaged in the near future, occultation measurements have already been used to resolve spatial scales of about 1 AU in the disk around T Tauri (Simon *et al.* 1996).

5. Discussion and Conclusions

In this paper, we have calculated SEDs from the outbursting accretion disk models of BLHK, using frequency-dependent radiative transfer and including disk-disk reprocessing. Previous workers have calculated SEDs for constant mass-flux disks by summing blackbody emission or stellar spectra over a $\overline{\tau} = 2/3$ surface. Our spectra also provide a good match for the observed SEDs of FU Orionis, V1057 Cygni, and V1515 Cygni. In our model, the flux at wavelengths

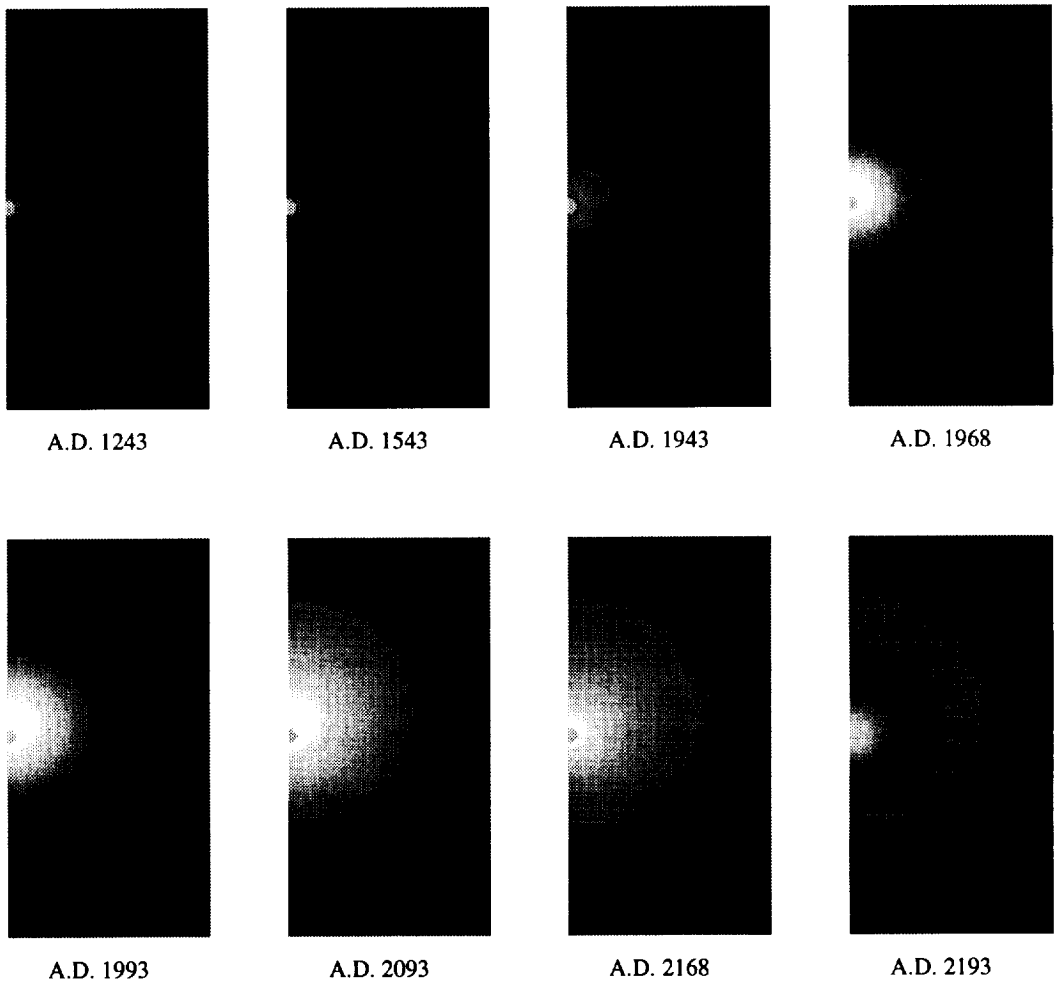

Fig. 6.— Time series showing the progress of an outburst cycle in the model V1515 Cygni (B1) disk, as seen through a B-band filter. All frames cover 0.3 AU in radius, and share one flux scale which spans 18 decades. The brightest regions represent a B-band flux through the disk surface of 1×10^{11} erg cm^{-2} s^{-1}. The disk is tipped away from the viewer by 30° from pole-on. The B1 model SED shown in Figure 4 was calculated using the 1993 disk model in the fifth frame. A full outburst cycle in this model lasts 1150 years.

0.35–2 μm is provided by the disk inside 0.25 AU. Flux at 2–5 μm is provided partly by the disk inside 0.25 AU, partly by reprocessing in the outer disk of luminosity from the inner disk, and partly by a flattened envelope in approximate radiative equilibrium with a central luminosity L_{il}. Flux at 5–100 μm is provided by the envelope.

Our model FU Orionis objects have some remaining weaknesses. Since the luminosities needed to match the envelope spectra differ somewhat from those available in the models for reprocessing by the envelope, it is likely the shape of the volcano is not accurately rendered by the disk models (§§ 2.3, 2.4). However, among the three objects, a higher required envelope illumination luminosity does correspond to a more open model volcano (§ 4.3). Another hint of mild inaccuracies in the disk models comes from Figure 4, where both A1 and B1 show excesses at 0.55 μm over the corresponding measured fluxes. While the B1 excess may be due to the 1980 dimming event in V1515 Cygni (§ 4.1), both excesses might also be removed if the steep shapes of the volcanos shown in Figure 2 were relaxed, reducing the small degree of reprocessing between the volcanos' opposite walls. Whether this relaxation is realistic could be demonstrated using two-dimensional hydrodynamic simulations of the outburst region, allowing radial derivatives of the physical quantities to act on the structure. The volcanos would be flatter also if the viscosity parameter α in the outburst region were larger than the value of 10^{-3} used in the BLHK models. The disk models further omit the back reaction of self-illumination on the propagation of the outburst, which is expected to be a second-order effect. Again in Figure 4, the spectrum of the C1 model is about 0.1 decade too faint at 3 μm, and 0.1 decade too bright at 5 μm. If the model were more luminous or its volcano were more open, so that reprocessing were stronger, this mis-fit might be corrected by increasing the radius of the hole in the envelope.

The model envelope is another area where further work is needed. Our model is an over-simplification chosen for the small number of parameters it introduces. Model envelopes could be generated using a two-dimensional radiation hydrodynamic collapse calculation, but the exploration of parameter space needed to find envelopes appropriate for the spectra would make this a large undertaking. However, reconciliation of the illumination luminosities with the central luminosities of the objects does require more realistic vertical density gradients in the envelope, such as would be obtained from collapse calculations.

The disk models assume a constant, low viscosity parameter $\alpha = 10^{-4}$ outside the outburst region. As discussed by BLHK, this small viscosity results in a disk which is self-gravitating for the given input mass fluxes at radii beyond about 1 AU, yet we extend the disks to radii of 100 AU and more. This clear inconsistency is perhaps justified because outside a radius R_h (0.8 AU in the largest case, the A1 model), the disk is invisible, hidden beneath the envelope. The thickness of the outer disk does affect the spectrum via the envelope temperature, which is a function of distance from the central object (equation 3). But this distance is only a weak function of the disk thickness, so any effect on the spectrum is small. The other requirement on the outer disk by the outburst model is that the outer disk supply mass at a near-constant rate; the mechanism of mass transport there might for example be gravitational instability, rather than that in the standard

Shakura & Sunyaev (1973) accretion disk picture.

Although the process which triggers the rapid rise-time outbursts of FU Orionis and V1057 Cygni is still not understood, work in this paper lends solid additional support to the hypothesis that a thermal accretion event in a protostellar disk is responsible for the outburst. The spectral fitting also shows that an optically thick dusty envelope is an important component of the system, required to fit the 5–100 μm region. The presence of the envelope underscores the relative youth of these objects. The calculations demonstrate that reprocessing of disk light by the disk itself can produce a surface temperature distribution $T \sim r^{-1/2}$, which would result in a flat spectrum in the $(\lambda, \lambda F_\lambda)$ diagram even without the envelope. However, this effect is cut off when the disk surface becomes concave towards the midplane. This occurs at a radius of about 10 AU, where the temperature at the surface $\overline{\tau} = 2/3$ reaches the ice condensation point. As a result, the envelope is still needed to explain the flat spectrum over the full observed range of wavelengths.

Finally, we note that many more details of the mechanism powering FU Orionis outbursts can be extracted from time-resolved spectroscopic observations. Though available data are sparse, it is already known that various spectral features appear and disappear during the evolution of the individual objects. Useful in the future would be spectra from 0.1–100 μm, spaced in time to resolve rapid changes in the light curve. For example, BBW76 is a recently-discovered FU Orionis object which is currently fading (Eislöffel, Hessman & Mundt 1990; Reipurth 1991). Once a light curve is available covering a sufficient fraction of an outburst, a disk model can be constructed for this object. Comparison of SEDs calculated from the model against those observed over time will provide an even more rigorous test of the validity of the outbursting accretion disk model.

These calculations were possible because David Alexander graciously calculated for us the frequency-dependent opacities. Scott Kenyon was quick to answer our questions. We also learned from discussions with Pat Cassen, Martin Cohen, Doug Lin and Diane Wooden, and the recommendations of an anonymous referee. The work was supported by grants NAGW–3408 and NAGW–4456 from the NASA Origins of Solar Systems Program, and by a special NASA theory program which supports a joint Center for Star Formation Studies at NASA–Ames Research Center, University of California, Berkeley, and University of California, Santa Cruz. The research made use of NASA's Astrophysics Data System Abstract Service, and the Simbad database, operated at CDS, Strasbourg, France.

REFERENCES

Adams, F. C., Lada, C., & Shu, F. H. 1987, ApJ, 312, 788

Adams, F. C., & Shu, F. H. 1986, ApJ, 308, 836

Adams, F. C., Lada, C. J., & Shu, F. H. 1988, ApJ, 326, 865

Alexander, D. R. 1995, private communication

Alexander, D. R., Auguson, G. C., & Johnson, H. R. 1989, ApJ, 345, 1014

Alexander, D. R., & Ferguson, J. W. 1994, ApJ, 437, 879

Bessell, M. S., & Brett, J. M. 1988, PASP, 100, 1134

Bell, K. R. 1997, in preparation

Bell, K. R., Cassen, P., Klahr, H., & Henning, Th. 1997, in preparation

Bell, K. R., & Lin, D. N. C. 1994, ApJ, 427, 987

Bell, K. R., Lin, D. N. C., Hartmann, L. W., & Kenyon, S. J. 1995, ApJ, 444, 376 (BLHK)

Bodenheimer, P., Yorke, H. W., Różyczka, M., & Tohline, J. 1990, ApJ, 355, 651

Calvet, N., Hartmann, L., & Kenyon, S. J. 1993, ApJ402, 623

Calvet, N., Patino, A., Magris, G. C., & D'Alessio, P. 1991, ApJ, 380, 617

Cohen, M. 1980, MNRAS, 191, 499

Colina, L., & Bohlin, R. C. 1994, AJ, 108, 1931

Cox, A. N., & Tabor, J. E. 1976, ApJS, 31, 271

Eislöffel, J., Hessman, F. V., & Mundt, R. 1990, A&A, 232, 70

Hartmann, L., & Kenyon, S. 1985, ApJ, 299, 462

Hartmann, L., & Kenyon, S., & Calvet, N. 1993, ApJ, 407, 219

Hartmann, L., Kenyon, S., & Hartigan, P. 1993, in Protostars and Planets III, eds. E. H. Levy & J. Lunine (Tucson: University of Arizona Press), p497

Herbig, G. 1966, Vistas in Astr. vol.8, eds A. Beer and K. Aa. Strand (Oxford: Pergamon), p109

Herbig, G. 1977, ApJ, 217, 693

Herbig, G. 1989, in ESO Workshop on Low Mass Star Formation and Pre-main-sequence Objects, ed. B. Reipurth (Garching: ESO), p233

Johnson, H. L. 1965, ApJ, 141, 923

Kawazoe, E., & Mineshige, S. 1993, PASJ, 45, 715

Kenyon, S. J., Calvet, N., & Hartmann, L. W. 1993 ApJ, 414, 676

Kenyon, S. J., & Hartmann, L. W. 1987, ApJ, 323, 714

Kenyon, S. J., & Hartmann, L. W. 1989, ApJ, 342, 1134

Kenyon, S. J., & Hartmann, L. W. 1991, ApJ, 383, 664

Kenyon, S. J., Hartmann, L. W., & Hewett, R. 1988, ApJ325, 231

Kenyon, S. J., Hartmann, L. W., & Kolotilov, E. A. 1991, PASP, 103, 1069

Kley, W., & Lin, D. N. C. 1996, ApJ, 461, 933

Lin, D. N. C., Hayashi, M., Bell, K. R., & Ohashi, N. 1994, ApJ, 435, 821

Lin, D. N. C., & Papaloizou, J. 1985, in Protostars and Planets II, eds. D. C. Black & M. S. Matthews (Tucson: University of Arizona Press), p981

Mathis, J. S. 1990, ARA&A, 28, 37

Mihalas, D. 1978, Stellar Atmospheres, 2d ed (San Francisco: W. H. Freeman)

Murdin, P., & Penston, M. V. 1977, MNRAS, 181, 657

Paczynski, B. 1976, QJRAS, 17, 31

Petrov, P. P., & Herbig, G. H. 1992, ApJ, 392, 209

Pollack, J. B., McKay, C., & Christofferson, B. 1985, Icarus, 64, 471

Pollack, J. B., Hollenbach, D., Beckwith, S., Simonelli, D. P., Roush, T., & Fong, W. 1994, ApJ, 421, 615

Racine, R. 1968, AJ, 73, 233

Reipurth, B. 1991, in IAU Symposium 137, Flare Stars in Star Clusters, Associations, and the Solar Vicinity (Dordrecht: Kluwer)

Ruden, S. P., & Pollack J. B. 1991, ApJ, 375, 740

Seaton, M. J. 1994, MNRAS, 266, 805

Shakura, N. I., & Sunyaev, R. A. 1973, A&A, 24, 337

Simon, M., Longmore, A. J., Shure, M. A., & Smillie, A. 1996, ApJ, 456, L41

Straizys, V., Meistas, E., Vansevicius, V., & Goldberg, E. P. 1989, A&A, 222, 82

Syer, D., & Clarke, C. 1996, MNRAS, 278, L23

Wooden, D. H. 1996, private communication

Wooden, D. H., Bell, K. R., Butner, H. M., and Goguen, J. D. 1995, BAAS, 187, 22.06

Yorke, H. W. 1979, A&A, 80, 308

Yorke, H. W. 1986, in Astrophysical Radiation Hydrodynamics, ed. K.-H. Winkler & M. L. Norman (Dordrecht: Reidel), 141

Yorke, H. W., Bodenheimer, P., & Laughlin, G. 1993, ApJ, 411, 274

Yorke, H. W., Bodenheimer, P., & Laughlin, G. 1995, ApJ, 443, 199

Mon. Not. R. Astron. Soc. **276**, 1179–1184 (1995)

A simple model for a buoyancy-driven dynamo in accretion discs*

Michał Różyczka,[1,2] Neal Joung Turner[3] and Peter Bodenheimer[3]
[1] *Warsaw University Observatory, Al. Ujazdowskie 4, PL-00478 Warszawa, Poland*
[2] *Nicolaus Copernicus Astronomical Center, Bartycka 18, PL-00716 Warszawa, Poland*
[3] *UCO/Lick Observatory, University of California, Santa Cruz, CA 95064, USA*

Accepted 1995 May 9. Received 1995 April 18

ABSTRACT

A model for the magnetic dynamo process in accretion discs is proposed that does not involve underlying turbulent motions. The key ingredient of the model is the magnetic buoyancy. Combined with Coriolis twist, the buoyant motions result in a backcoupling between azimuthal and radial components of the field. It is shown that for reasonable values of the free parameters of the model all three components of the magnetic field reach a stable saturation state consistent with the basic assumptions underlying the model.

Key words: accretion, accretion discs – MHD.

1 INTRODUCTION

To amplify and maintain an originally weak magnetic field, the classical kinematic dynamo model (see e.g. Parker 1979, Section 19) employs both a regular large-scale and a chaotic small-scale (turbulent) velocity field. The large-scale velocity field is just rotation, whereas the turbulent velocities are usually associated with thermal convection. As a by-product of the dynamo action, a fluctuating small-scale magnetic field is created, whose amplitude is assumed to be much smaller than the characteristic intensity of the large-scale (mean) field. Another key assumption of the model is that both large-scale and turbulent flows are not affected by magnetic fields. Pudritz (1980), who calculated non-linear effects for a kinematic dynamo in an accretion disc, found, however, that fluctuating fields much more energetic than the mean field develop, strongly reducing the intensity of turbulent motions. As a result, the mean field cannot grow above a certain critical value, at which the turbulence is shut down. The mean field was estimated to saturate at $\beta < 75$ (where β is the ratio P_g/P_m of gas to mean field magnetic pressure), i.e. far away from the thermal equipartition value of $\beta = 1$ suggested as a natural dynamo limit (Galeyev, Rosner & Vaiana 1979). Recently, more serious problems with the classical dynamo have been reported. A study of the Galactic dynamo by Kulsrud & Anderson (1992) revealed that rapidly growing fluctuating fields may substantially modify the turbulent flow before any significant amplification of the mean field is achieved. A similar pessimistic conclusion was reached in a general study of astrophysical kinematic dynamos by Vainshtein & Cattaneo (1992): fluctuating magnetic fields are readily generated at tiny scales (where they reach equipartition values), while the mean field remains extremely weak.

Objections against the kinematic dynamo have also been raised by Hawley & Balbus (1992), who note that the classical model may not be applicable to accretion discs, as in that case even weak fields are able to significantly influence the fluid flow, thus invalidating the assumption on which the kinematic dynamo is based. This effect is due to the magnetorotational instability (hereafter MRI, a term coined by Goodman & Xu 1994), whose importance has been revealed in a series of papers by Balbus & Hawley (see Hawley, Gammie & Balbus 1995 and references therein). Yet another, long-known objection against the kinematic dynamo in accretion discs is that the origin of the turbulent velocity field remains unknown. The only commonly accepted source of turbulent motions in accretion discs, the convective instability, is usually effective in limited regions of a disc only (see e.g. Stella & Rosner 1984), and thus it cannot solve the problem.

The idea that magnetic fields could be amplified without any assumed (or underlying) turbulence is not new. Its origin goes back to the early 1970s, when it was noted that the magnetic buoyancy, which is capable of generating turbulent motions by itself, might be an important factor in the dynamo process (Parker 1971). Meyer & Meyer-Hofmeister (1983) were the first to employ that idea for an estimate of the saturation state parameters in accretion discs. The effect of magnetic buoyancy on accretion discs was also discussed by Galeyev et al. (1979) and Stella & Rosner (1984). The first complete disc dynamo model entirely independent of any underlying turbulence was proposed by Tout & Pringle (1992). In that model, the Parker instability (Parker 1979, sections 13.4 and 13.5) due to the azimuthal field com-

* UCO/Lick Observatory Bulletin No. 1318.

ponent, and the magnetorotational instability due to the vertical field component are employed to close the dynamo loop. Almost simultaneously, a Galactic dynamo model based on magnetic buoyancy was proposed by Parker (1992). Finally, in a recent stellar dynamo model of Tout & Pringle (1995) the dynamo feedback is provided by the differential stellar rotation combined with 'turnover flows' generated by magnetic buoyancy.

Based on the above discussion, we find that a dynamo able to amplify magnetic fields without any underlying chaotic small-scale motions is a very promising idea. In particular, under the conditions characteristic of an accretion disc interior (strong shear, strong vertical stratification due to variable gravitational acceleration in the direction perpendicular to the mid-plane) a dynamo powered by hydromagnetic instabilities that tap the energy directly from the orbital motion becomes a possible solution to all problems of the classical kinematic scenario. In the present paper we discuss a simple disc dynamo model based on processes outlined in a recent paper by Różyczka, Bodenheimer & Lin (1995), who performed a numerical study of buoyancy effects in accretion discs. Our approach is generally similar to that of Tout & Pringle (1992, 1995). For reasons explained in Section 2, however, we do not rely on the MRI to close the dynamo loop, and the dynamo feedback is provided by magnetic buoyancy and helicity of the motions the buoyancy induces. We also differ from Tout & Pringle in the assumptions concerning the field loss from the disc, for which we assume a more general form. Our dynamo is described by a set of equations which are introduced and discussed in Section 2. The solutions of the dynamo equations are presented in Section 3. In Section 4 we summarize the results and discuss their implications for the structure and dynamics of an accretion disc.

2 THE DYNAMO EQUATIONS

To explain the physical basis of our model we shall begin with a brief summary of the simulations performed by Różyczka et al. (1995), who have followed the evolution of a seed poloidal field in an accretion disc under the assumption of axial symmetry. They find that the azimuthal component of the field B_ϕ grows due to shear until the thermal equipartition value of $\beta = 1$ is approached. The growth of B_ϕ is stopped by formation of buoyant plumes with vigorous internal motions, leading eventually to partial ejection of the field from the disc, fragmentation of the seed and the establishment of a turbulent velocity field. Shortly afterwards a quasi-stationary state is reached, in which the poloidal field assumes a patchy structure, with the medium between patches being either more weakly magnetized than the patches themselves or entirely field-free.

Różyczka et al. (1995) argue that the patches are likely to follow the same evolutionary pattern as the initial seed, and they point out that if the assumption of axial symmetry were relaxed, the Coriolis force acting on buoyant elements of disc gas would result in helical twisting of the azimuthal field lines and amplification of the poloidal field. An example of three-dimensional effects that could counteract the dynamo action instead of supporting it is given by Hawley et al. (1995), who find that weak azimuthal fields are prone to the MRI which results in magnetoturbulence. Therefore, it is conceivable that B_ϕ could saturate far below the thermal equipartition value, before magnetic buoyancy becomes important. Hawley et al. (1995) point out, however, that as time advances the wavelength of the dominant azimuthal mode of the MRI becomes longer, and indeed their fig. 8 shows the field organizing itself into more coherent structures which may eventually evolve into nearly axisymmetric patches.

The simulations of Różyczka et al. (1995) indicate that, because of the patchy structure of the poloidal field in the saturated state, the MRI would not significantly influence the vertical component of the field B_z, and that the generation of the radial component B_r from B_z due to MRI would be rather inefficient. Thus we assume that the key link in the dynamo loop is not the $B_z \rightarrow B_r$ transformation due to the MRI [as proposed by Tout & Pringle (1992)], but the $B_\phi \rightarrow B_r$ transformation due to the helical twisting of B_ϕ lines. Further discussion of this issue is deferred to Section 4. Here we would only point out that the MRI is by no means unimportant in our scenario, as it causes the magnetized region to spread radially, resulting in the expansion of an initially localized dynamo process both towards the centre of the disc and towards its outer edge.

Both Różyczka et al. (1995) and Hawley et al. (1995) find that the field is likely to change its orientation on a length-scale which is small compared with the disc thickness. This finding corroborates another assumption made by Tout & Pringle (1992), according to which the main source of magnetic flux loss within the disc is reconnection. Since, however, according to Różyczka et al. (1995) and Hawley et al. (1995) *all three* field components may change sign on scales that are small in *at least one direction*, we do not restrict reconnection to B_z [as was done by Tout & Pringle (1992)], but allow for it also in the case of B_ϕ and B_r.

Following Tout & Pringle (1992), we write our equations in terms of B_ϕ, B_z and B_r, which should be regarded as local average values of the field components. As indicated in the preceding paragraph, we assume that every component of the field is destroyed by reconnection. The reconnection proceeds at a rate given by the ratio of the momentary value of the component and an appropriate time-scale $\tau_{\rm rec}$ (which may be different for different components). Additionally, and in accordance with Tout & Pringle (1992), B_ϕ and B_r are lost from the surface of the disc due to the undulating modes of the Parker instability (Parker 1979, Section 13) at rates given by the ratios of their momentary values to a buoyant time-scale $\tau_{\rm p}$.

We assume that the disc is nearly Keplerian. Thus, B_ϕ is created from B_r due to shear at a rate

$$\frac{{\rm d}B_\phi}{{\rm d}t} = \frac{3\pi}{T} B_r , \tag{1}$$

where T is the local Keplerian orbital period. The same Parker instability that results in loss of B_ϕ and B_r from the disc generates the vertical component of the field at a rate

$$\frac{{\rm d}B_z}{{\rm d}t} = \frac{B_\phi}{\tau_{\rm p}} + \frac{B_r}{\tau_{\rm p}} . \tag{2}$$

The gain terms given by equations (1) and (2) are the same as in Tout & Pringle (1992). To complete the dynamo we have to define the rate at which the radial field is generated from

B_ϕ. Our key assumption is that the buoyant elements acquire an angular speed equal to the epicyclic frequency κ. As in a Keplerian disc κ is equal to the local angular orbital velocity Ω, we effectively assume that the azimuthal field lines within the element are rotated on a time-scale of the local orbital period, i.e. that B_r is generated at a rate

$$\frac{\mathrm{d}B_r}{\mathrm{d}t} = \frac{B_\phi}{T}. \tag{3}$$

Admittedly, this may seem to be an overestimate. Our B_r generation rate is not, however, greater than that found by Tout & Pringle (1992), and furthermore the saturation value of our dominant field component (B_ϕ) turns out to be only weakly dependent on this assumed rate (see below). Assembling all gain and loss terms for each field component we obtain the final set of equations

$$\frac{\mathrm{d}B_\phi}{\mathrm{d}t} = \frac{3\pi}{T} B_r - \frac{B_\phi}{\tau_\mathrm{p}} - \frac{B_\phi}{\tau_\mathrm{rec}^\phi}, \tag{4}$$

$$\frac{\mathrm{d}B_r}{\mathrm{d}t} = \frac{B_\phi}{T} - \frac{B_r}{\tau_\mathrm{p}} - \frac{B_r}{\tau_\mathrm{rec}^r}, \tag{5}$$

$$\frac{\mathrm{d}B_z}{\mathrm{d}t} = \frac{B_\phi}{\tau_\mathrm{p}} + \frac{B_r}{\tau_\mathrm{p}} - \frac{B_z}{\tau_\mathrm{rec}^z}, \tag{6}$$

in which the buoyant and recombination time-scales have yet to be specified.

If $B_\phi \gg B_r$, the characteristic time-scale of buoyant motions is given by

$$\tau_\mathrm{p} = \eta \frac{H}{V_\mathrm{A}^\phi}, \tag{7}$$

where H is the half-thickness of the disc given by the standard expression

$$H = \frac{\sqrt{2}c_s}{\Omega}, \tag{8}$$

V_A^ϕ is the Alfvén velocity calculated from B_ϕ, and η is a parameter in the range 2–5 (Tout & Pringle 1992). When we integrated the equations with the formula (7) for τ_p, it turned out that B_r approached $0.5B_\phi$ in the saturation state, which prompted us to adopt a more general, heuristic expression

$$\tau_\mathrm{p} = \eta \frac{H}{V_\mathrm{A}^\phi + V_\mathrm{A}^r}, \tag{9}$$

where V_A^r is the Alfvén velocity calculated from B_r. That modification, however, did not result in any significant changes in the saturation state.

The characteristic time-scales for reconnection, $\tau_\mathrm{rec}^{\phi,r}$, of the azimuthal and radial fields are defined as

$$\tau_\mathrm{rec}^{\phi,r} = \frac{\delta z}{\Gamma} \frac{1}{V_\mathrm{A}^{\phi,r}}, \tag{10}$$

where δz is an average vertical size (thickness) of a magnetized patch, and Γ is a parameter related to the magnetic Reynolds number, in the range of 0.02–0.1 (Tout & Pringle 1992). In the following, an effective thickness Δz will be consistently used instead of the ratio $\delta z/\Gamma$. Following Tout & Pringle (1992) we assume that the vertical field can reconnect both in the ϕ and r directions, on characteristic time-scales $\tau_\mathrm{rec}^{z\phi}$ and τ_rec^{zr}, respectively. The effective reconnection time-scale τ_rec^z is then given by

$$(\tau_\mathrm{rec}^z)^{-1} = (\tau_\mathrm{rec}^{z\phi})^{-1} + (\tau_\mathrm{rec}^{zr})^{-1}. \tag{11}$$

Both $\tau_\mathrm{rec}^{z\phi}$ and τ_rec^{zr} are defined analogously to $\tau_\mathrm{rec}^{\phi,r}$ in equation (10), with Δz replaced by characteristic length-scales $\lambda_\mathrm{rec}^{z\phi}$ and $\lambda_\mathrm{rec}^{zr}$ for the reconnection of the vertical field in the ϕ and r directions, respectively. For an estimate of $\lambda_\mathrm{rec}^{zr}$ we modify the prescription of Tout & Pringle (1992) (their formulae 2.3.2 and 2.3.4–2.3.6) to obtain

$$\lambda_\mathrm{rec}^{zr} = \frac{2}{3\sqrt{2}} \frac{1}{\eta} \frac{V_\mathrm{A}^\phi}{c_s} \Delta z, \tag{12}$$

where Δz replaces the MRI length-scale. Provided that the wavelength of the buoyant instability in the azimuthal direction is shorter than the characteristic azimuthal extent of a magnetized patch, i.e. that the patch undulates along its azimuthal extent [which we expect to happen based on simulations reported by Różyczka et al. (1995)], we may simply approximate $\lambda_\mathrm{rec}^{z\phi}$ by Δz. Finally, we relate Δz to H by the formula

$$\Delta z = \epsilon H, \tag{13}$$

where ϵ is a free parameter which, given the range of Γ in equation (10), could in principle vary in the range $0 < \epsilon \leq 10$ (at $\epsilon = 10$ the average geometrical thickness of a patch δz approaches H). However, independently of the field strength, there is always a small-scale structure clearly visible in meridional cross-sections of both the Hawley et al. (1995) and Różyczka et al. (1995) models, indicating that δz in excess of $\sim 0.1H$ is rather unlikely. On the other hand, very small ϵ results in extremely large loss terms in equations (14)–(16), practically inhibiting the dynamo effect. For these two reasons, we restrict ϵ to vary between 0.1 and 1.0, i.e. we assume that the upper limit for the characteristic scale of magnetic structures generated in the disc is of the order of $0.1H$.

Taking T as a unit of time, and $c_s\sqrt{4\pi\rho}$ (where ρ is the local density) as a unit of magnetic field intensity, we can rewrite equations (4)–(6) in the form

$$\frac{\mathrm{d}b_\phi}{\mathrm{d}t'} = 3\pi b_r - \frac{\sqrt{2}\pi}{\eta} b_\phi (b_\phi + b_r) - \frac{\sqrt{2}\pi}{\epsilon} b_\phi^2 \tag{14}$$

$$\frac{\mathrm{d}b_r}{\mathrm{d}t'} = b_\phi - \frac{\sqrt{2}\pi}{\eta} b_r (b_\phi + b_r) - \frac{\sqrt{2}\pi}{\epsilon} b_r^2 \tag{15}$$

$$\frac{\mathrm{d}b_z}{\mathrm{d}t'} = \frac{\sqrt{2}\pi}{\eta} (b_\phi + b_r)^2 - \frac{\sqrt{2}\pi}{\epsilon} b_z^2 \left(1 + \frac{3\sqrt{2}}{2} \frac{\eta}{b_\phi}\right), \tag{16}$$

where time t' and field components b_ϕ, b_r and b_z are now expressed in the units defined above. We decided not to incorporate the numerical factor of $\sqrt{2}\pi$ into the parameters ϵ and η in order to preserve their straightforward relation to the disc half-thickness H.

3 SOLUTION OF THE DYNAMO EQUATIONS

The set of ordinary differential equations consisting of equations (14)–(16) was integrated numerically using the fifth-order Runge–Kutta method with adaptive stepsize control, as implemented in the Numerical Recipes routine ODEINT (Press et al. 1992), until an equilibrium (saturation) state was reached. To examine dependence of the equilibrium fields on initial conditions, numerical integrations were carried out for a wide variety of small initial fields. Fig. 1 shows the results for initial fields, in units of $c_s\sqrt{4\pi\rho}$, of $b_\phi = b_r = b_z = 10^{-2}$, 10^{-6} and 10^{-12}, with $\eta = 2.5$ and $\epsilon = 0.1$. The system moves to the same equilibrium in each case – that is, the saturation field does not depend on the strength of the initial field. Additionally, analytic equilibrium solutions to equations (14)–(16) were found by setting time derivatives to zero and solving the resultant set of three algebraic nonlinear equations. We found that the set has only one real, non-zero solution. For the (η, ϵ) pairs checked, the equilibrium values returned by the numerical integrator agree with the analytic solution to better than four significant digits.

As a test of the stability of the equilibria, the integration was also run with initial conditions both larger and smaller than the equilibrium values by 1 per cent. The system came to the same equilibria as in the cases with small initial fields, i.e. the saturated state of the dynamo proved to be stable.

To show the dependence of the saturation field on the two parameters η and ϵ, numerical integrations were run to equilibrium over a grid of (η, ϵ) combinations. The grid is 11 points on a side, evenly spaced in η and in $\log_{10}\epsilon$, and covers the region where $2 \le \eta \le 5$ and $0.1 \le \epsilon \le 1$. The results are plotted in Fig. 2, and selected points are listed in Table 1. As can be seen in Fig. 2, the strongest component of the field at saturation is b_ϕ, with b_r smaller by a factor of about 2. For $\epsilon = 1$, b_z is only slightly smaller than b_r. When $\epsilon = 0.1$, b_z is less than b_r by 1–1.5 orders of magnitude. Also from inspection of Fig. 2, dependence of the field components on η is weak, because the largest loss terms are the reconnection ones, which are determined by ϵ.

To demonstrate the importance of the reconnection terms, we removed them from the b_ϕ and b_r equations (14) and (15), and repeated the integrations. The much smaller remaining loss terms due to the Parker instability led to large intensities of saturation fields, such that the magnetic pressure was comparable with or larger than the gas pressure over the (η, ϵ) region examined. For example, for $\eta = 2.5$ and $\epsilon = 0.3$, the results were $b_\phi = 1.3$, $b_r = 0.42$ and $b_z = 0.27$.

Finally, we examined the sensitivity of the saturation fields to the Coriolis gain term in the b_r equation (15) by increasing it by a factor of 2. As a result, the value of the dominant component b_ϕ increased by a factor of 1.25, while b_r and b_z changed by factor of 1.6–1.7. Effects of comparable magnitude but opposite sign were observed in another integration, with the Coriolis term decreased by a factor of 2.

4 SUMMARY AND DISCUSSION

We demonstrated that our dynamo equations yield stable saturation states to which the amplification process converges after a few Keplerian periods. The saturated field strength is independent of the initial seed field strength. It does depend, however, on two parameters, one characterizing the growth time of undulations on azimuthal field lines (η), and the other the average thickness of magnetized patches in the meridional plane of the disc (ϵ). Slowly

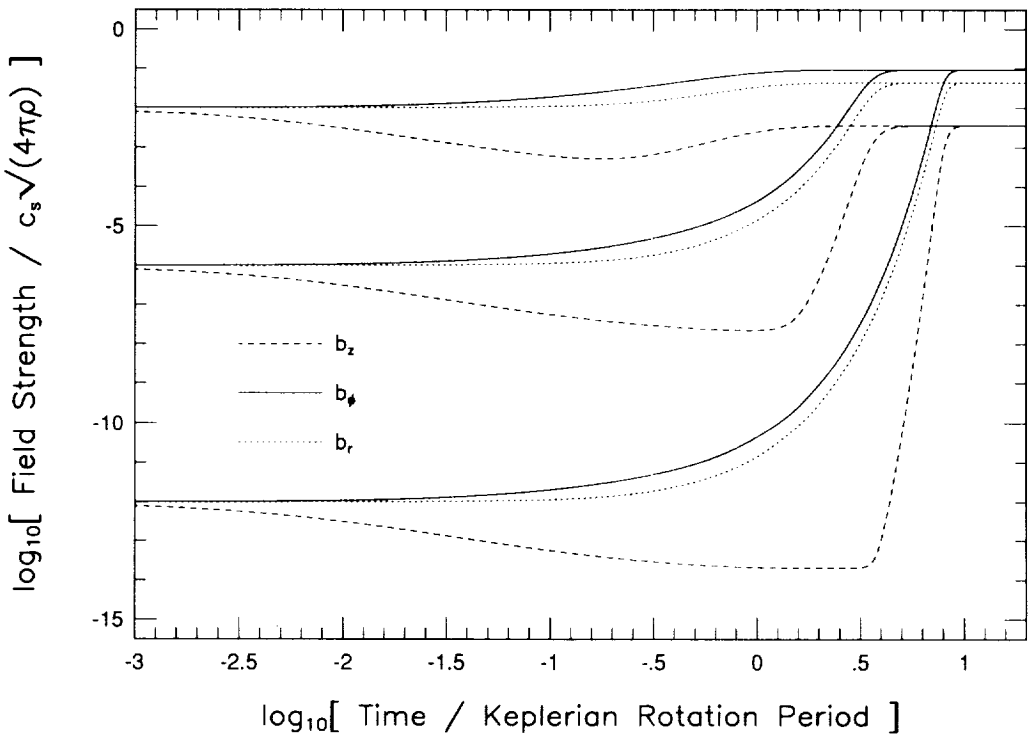

Figure 1. The convergence of the solutions of the dynamo equations to a unique saturation state.

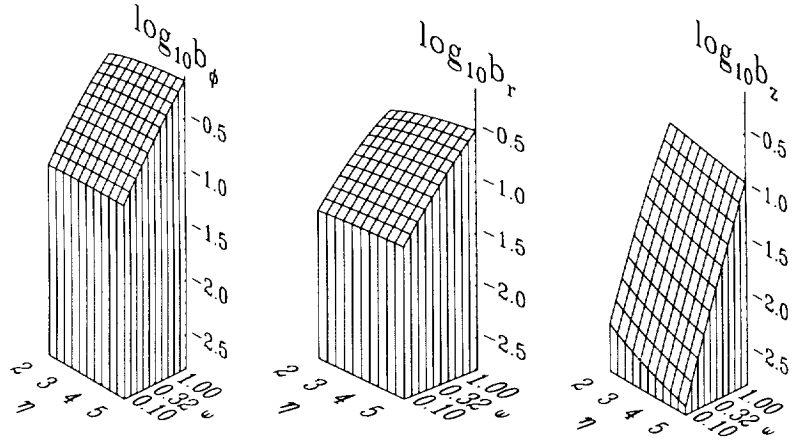

Figure 2. The dependence of saturation field components on the parameters η and ϵ. Fields are in units of $c_s\sqrt{4\pi\rho}$.

Table 1. Saturation field strengths versus Parker time-scale parameter η and reconnection parameter ϵ. Fields are in units of $c_s\sqrt{4\pi\rho}$. Starting field components in each case were $b_\phi = b_r = b_z = 10^{-12}$

η	ϵ	b_ϕ	b_r	b_z
2	0.1	0.091	0.042	0.0043
2	0.3	0.23	0.10	0.029
2	1	0.50	0.20	0.16
2.5	0.1	0.093	0.043	0.0036
2.5	0.3	0.24	0.11	0.025
2.5	1	0.56	0.23	0.15
5	0.1	0.097	0.045	0.0019
5	0.3	0.27	0.12	0.015
5	1	0.72	0.31	0.12

growing undulations (large η) lead to smaller surface loss rates of B_ϕ and B_r, and to larger saturation values of those two components. On the other hand, the rate of B_z generation is lower for larger η, resulting in a smaller saturation value. The dependence of the saturation state on η is rather weak, however; the effect of changing ϵ is much more strongly pronounced. Smaller ϵ enhances the reconnection loss and results in a general decrease of the saturated field strength.

We showed that with reconnection loss terms removed from the B_ϕ and B_r equations (equations 14 and 15) the field saturates at high values corresponding to $\beta \leq 1$. Let us note that at $\beta \approx 1$ the Alfvén velocity, which may be regarded as a reasonable approximation of buoyancy-generated velocities (Meyer & Meyer-Hofmeister 1983; Tout & Pringle 1992, 1995) is comparable with the velocity of sound c_s. The characteristic time-scale for the escape of the field from the disc is then $H/c_s \approx 1/\Omega$. Moreover, for $\beta < 1$ a rapid increase of dissipation due to shock waves (not accounted for in our model) is expected. Thus, $\beta = 1$ seems to be a reasonable natural limit to field amplification. It may be noted that the same conclusion was reached in the case of a kinematic (convective) disc dynamo by Galeyev et al. (1979), who pointed out that at $\beta < 1$ the effects of magnetic tension would become strong enough to significantly suppress the convection. Our conclusion is that both the reconnection terms discussed in the present paragraph should be retained in the dynamo equations.

In the saturation state the strongest component is B_ϕ, with B_r generally smaller by a factor of ~ 2, and B_z smaller by another factor of 3–10. Thus the structure of the field in the saturation state is entirely different from that obtained by Tout & Pringle (1992), who found $B_z \approx B_\phi$ and $B_r \approx 0.15 B_\phi$. It is, however, consistent with the assumed structure of the field, which in a meridional cross-section of the disc may be described as an ensemble of radially elongated patches with B_r constituting the main component of the poloidal field, and with the azimuthal field being still stronger. (Let us note that a patch of the poloidal field in the meridional plane corresponds to a bundle of toroidal field lines.) The basic uncertainty of our model concerns the Coriolis gain term in the B_r equation. We showed that an increased efficiency of B_r generation results in a relative increase of B_r with respect to B_ϕ, while a decreased efficiency results in a relative decrease of B_z with respect to B_ϕ. Since at the standard efficiency of Coriolis twist introduced in Section 2 B_r seems to be already rather strong, and B_z rather weak compared with B_ϕ, we conclude that the Coriolis twist rate should not differ much from the assumed value of $1/T$ if a saturated field with dominant B_ϕ and non-negligible B_z is to be obtained.

Its simplicity notwithstanding, our model produces entirely coherent results. First of all, reasonable saturated field strengths, somewhat below thermal equipartition, are obtained from reasonable assumptions concerning the range in which η and ϵ are allowed to vary. Secondly, the saturation values of all field components become consistently smaller with decreasing ϵ, which means that fields with significant small-scale structure are weak. This is exactly what one expects, as at a lower field intensity the magnetic tension is weak and the field lines may easily be wound up very tightly. Thirdly, the saturated field remains constant in time, as opposed to the Tout & Pringle (1992) model in which the

saturated field oscillates on an approximately orbital timescale with an amplitude reaching ~60 per cent of the mean value. Fourthly, as mentioned by Różyczka et al. (1995), even though our model involves turbulent motions it is free from the basic problem of the turbulent kinematic dynamos that have been raised by Kulsrud & Anderson (1992) and Vainshtein & Cattaneo (1992). While in the kinematic dynamo the turbulence may prevent amplification of the mean field, in the buoyant dynamo it does not set in until the azimuthal field has become strong enough to induce buoyant motions.

Tout & Pringle (1992) obtain an oscillating field because of the shut-off of the MRI at high B_z, resulting in a vanishing gain term in the B_r equation (B_r generation is resumed as soon as B_z falls below a critical value due to continuous reconnection). For the shut-off to occur, however, the B_z lines should extend throughout the whole thickness of the disc (connecting, possibly, to an external field). On the basis of numerical simulations reported by Hawley et al. (1995) and Różyczka et al. (1995) we feel, however, that the internal disc field is more likely to be organized in rather thin and flat, radially extended patches. The effect of the MRI acting on a patch is just radial stretching, and there is no chance for a shut-off to occur. Thus we feel that the scenario proposed by Tout & Pringle (1992) is more appropriate for a disc permeated by an externally connected vertical field. If such a field is absent, i.e. if one is interested in amplification of purely internal disc fields, our scenario seems to be more appropriate.

In conclusion we would like to stress that the simple model presented here is not so much meant to represent real astrophysical discs as to draw attention to hitherto unexplored possibilities. We merely demonstrated that a self-consistent scenario for field amplification and maintenance in accretion discs based on magnetic buoyancy and Coriolis effects is possible, and we believe that further research on this subject is highly desirable.

ACKNOWLEDGMENTS

This work was performed under the auspices of a special NASA theory programme which supports a joint Center for Star Formation Studies at NASA-Ames Research Center, University of California, Berkeley, and University of California, Santa Cruz. Further support was provided by grant NAGW-3408 from the NASA Origins of Solar Systems Program. MR acknowledges the support of the Committee for Scientific Research through the grant 2P 304 017 07.

REFERENCES

Galeyev A. A., Rosner R., Vaiana G. S., 1979, ApJ, 229, 318
Goodman J., Xu G., 1994, ApJ, 432, 213
Hawley J. F., Balbus S. A., 1992, ApJ, 400, 595
Hawley J. F., Gammie C. F., Balbus S. A., 1995, ApJ, 440, 742
Kulsrud R. M., Anderson S. W., 1992, ApJ, 396, 606
Meyer F., Meyer-Hofmeister E., 1983, A&A, 128, 420
Parker E. N., 1971, ApJ, 168, 239
Parker E. N., 1979, Cosmical Magnetic Fields. Oxford Univ. Press, Oxford
Parker E. N., 1992, ApJ, 401, 137
Press W. H., Teukolsky S. A., Vetterling W. T., Flannery B. P., 1992, Numerical Recipes in C, 2nd ed. Cambridge Univ. Press, Cambridge
Pudritz R. E., 1980, MNRAS, 195, 881
Różyczka M., Bodenheimer P., Lin D. N. C., 1995, ApJ, submitted
Stella L., Rosner R., 1984, ApJ, 277, 312
Tout C. A., Pringle J. E., 1992, MNRAS, 259, 604
Tout C. A., Pringle J. E., 1995, MNRAS, 272, 528
Vainshtein S. I., Cattaneo F., 1992, ApJ, 393, 165

THE ASTROPHYSICAL JOURNAL, 459:371–383, 1996 March 1

A NUMERICAL STUDY OF MAGNETIC BUOYANCY IN AN ACCRETION DISK[1]

MICHAŁ RÓŻYCZKA,[2,3] PETER BODENHEIMER,[4] AND D. N. C. LIN[4]

Received 1995 May 1; accepted 1995 September 12

ABSTRACT

We follow the evolution of a closed loop of relatively weak poloidal magnetic field, originally embedded somewhat above the midplane in a hydrostatic accretion disk. The equations of magnetohydrodynamics are solved on a numerical grid in axisymmetric geometry. Viscous heating, radiative transfer, and the horizontal and vertical components of the gravity of the central star are taken into account. As the evolution proceeds, toroidal field is built up as a result of shear in the disk, and the field becomes buoyant as a result of interchange modes of the Parker instability. The effective wavelength of the buoyant instability, and its dependence on the strength of the initial field loop, are found to be consistent with a linear stability analysis. The buoyancy results in turbulent motions and expulsion of some field from the disk. Eventually, a saturation state is reached, in which the field assumes a patchy structure, and the ratio of gas to magnetic pressure stabilizes in the range 1–5. Outward angular momentum transfer and an accompanying radial expansion of the magnetized region occur as a result of magnetic torques, and an equivalent α-viscosity parameter is estimated. The implications of these results on the generation of a magnetic dynamo in a disk are discussed.

Subject headings: accretion, accretion disks — instabilities — MHD

1. INTRODUCTION

The observational evidence for magnetic fields in accretion disks is in most cases circumstantial. The only disk for which measurements of magnetic field strength have been made is the primitive solar nebula, with fields of 0.1–1.0 G estimated from the residual magnetization of carbonaceous meteorites (Brecher 1972; Butler 1972). However, there are good reasons to believe that accretion disks are permeated by fields of either external or internal origin. In the first case, the field can be generated by the central object (Shu et al. 1994, and references therein) or dragged into the disk from the ambient medium (Lubow, Papaloizou, & Pringle 1994, and references therein). In the second case, the disk itself generates and maintains the field, owing to the dynamo effect (Tout & Pringle 1992, and references therein). In this paper we concentrate on the latter possibility.

While it was pointed out almost a quarter of a century ago that torques from internal fields could be responsible for the anomalously high effective viscosity of accretion disks (Shakura & Sunyaev 1973), the details of the actual processes are still not too well understood. An important advance was made in a series of papers by Balbus & Hawley (see Hawley, Gammie, & Balbus 1995, and references therein, hereafter the series is referred to as BGH). These papers deal with a magnetorotational (term coined by Goodman & Xu 1994) instability that is able to amplify originally weak disk fields of external origin by up to several orders of magnitude, and to induce ordered "two-channel" flow (Hawley & Balbus 1992) accompanied by an efficient angular momentum transfer. However, the more likely nonlinear outcome of the instability was found to be a hydromagnetic turbulence, for which the Shakura & Sunyaev effective viscosity parameter α ranged from 0.02 to 0.7, depending on the initial configuration assumed for the field. The most important conclusion of BGH is that with the help of magnetic fields one can induce both turbulence and angular momentum transfer in hydrodynamically stable regions of accretion disks. There are, however, two important physical effects that are not included in the simulations presented by BGH: magnetic buoyancy and resistivity. As the authors write, "buoyancy effects will undoubtedly have an important effect on the ultimate nonlinear fate of the disk" (Hawley & Balbus 1992).

Hawley & Balbus (1992) also note that the classical kinematic dynamo model (Parker 1979, § 19) may not be applicable to the amplification of internal fields in accretion disks, since even weak fields are able to significantly influence the fluid flow, thus invalidating the assumption on which the kinematic dynamo is based. Another, long-known objection against the kinematic dynamo in accretion disks is that its operation requires an underlying turbulent velocity field maintained by an essentially unidentified factor. The only commonly accepted source of turbulent motions in accretion disks, the convective instability, is usually effective in only limited regions of a disk (see, e.g., Stella & Rosner 1984), and thus it cannot solve the problem. The idea that the magnetic buoyancy might be an important factor in the dynamo process was formulated by Parker (1971). Meyer & Meyer-Hofmeister (1983) were the first to employ that idea for an estimate of the saturation state parameters in accretion disks. The effect of magnetic buoyancy on accretion disks was also discussed by Galeyev, Rosner, & Vaiana (1979) and Stella & Rosner (1984). The first complete disk dynamo model entirely independent of any assumed turbulence was proposed by Tout & Pringle (1992). In that model, the Parker instability (Parker 1979, §§ 13.4 and 13.5), arising from the azimuthal field component, and the magnetorotational instability, arising from the vertical field component, are employed to close the dynamo loop. Almost simultaneously, a Galactic dynamo model based on magnetic buoyancy was proposed by Parker (1992). Finally, in a recent stellar dynamo model of Tout & Pringle (1995), the

[1] UCO/Lick Observatory Bulletin, No. 1324.

[2] Warsaw University Observatory, Al. Ujazdowskie 4, PL-00478 Warszawa, Poland; mnr@hydra.astrouw.edu.pl.

[3] Copernicus Astronomical Center, ul.Bartycka 18, PL-00716 Warszawa, Poland.

[4] University of California Observatories/Lick Observatory, Board of Studies in Astronomy and Astrophysics, University of California, Santa Cruz, CA 95064; peter@lick.ucsc.edu.

dynamo feedback is provided by the differential stellar rotation combined with "turnover flows" generated by magnetic buoyancy.

Recently, the classical kinematic dynamo has also been questioned for reasons quite independent of the BGH conclusions concerning significant dynamic effects of weak fields in accretion disks. A study of the Galactic dynamo by Kulsrud & Anderson (1992) revealed that rapidly growing fluctuating fields may substantially modify the turbulent flow before any significant amplification of the mean field is achieved. A similar pessimistic conclusion was reached in a general study of astrophysical kinematic dynamos by Vainshtein & Cattaneo (1992): fluctuating magnetic fields are readily generated at tiny scales (where they reach equipartition values), while the mean field remains extremely weak. Again, under the conditions characteristic of an accretion disk interior (strong shear and strong vertical stratification owing to variable gravitational acceleration in the direction perpendicular to the midplane), a dynamo which is powered by hydromagnetic instabilities, and does not require any underlying turbulence to operate, becomes a possible solution to the problem.

Based on the above discussion, we expect the magnetic buoyancy to play a very important role in accretion disks. The buoyancy can modify significantly the magneto-rotational instability investigated by BGH, and it can contribute in a significant (possibly even dominant) way to the processes that amplify and maintain the internal magnetic field of a disk. Last but not least, it may be a crucial factor responsible for the generation of the disk's corona (Galeyev et al. 1979). The latter issue, however, will not be considered here. The aim of the present paper is to follow the development of the buoyant magnetic instability in a realistic accretion disk environment, taking into account as much physics as possible given limited numerical methods and computational resources. In particular, we attempt to find answers to the following questions:

1. What are the physical details of the processes that transform the primary orbital energy into the field and kinetic energies?
2. Is the magnetic buoyancy indeed a vital factor limiting the growth of the field inside the disk, as suggested by Galeyev et al. (1979)?
3. Can the magnetization initiated by a weak seed field of limited extent spread over large regions of the disk?
4. How sensitive are the properties of the saturated state to assumed initial conditions (seed field strength and location)?
5. Can the effective viscosity of a magnetic disk be estimated?

To that end, we perform numerical simulations of the evolution of a seed field in an accretion disk under the assumptions of axial symmetry and ideal magnetohydrodynamics. The technical details of the simulations are discussed in § 2. The results are presented in § 3, which also contains a discussion of physical processes responsible for the evolution of the seed field and a linear stability analysis. The results are summarized and discussed in § 4, together with some prospects for future research.

2. SIMULATIONS: TECHNICAL DETAILS

Following the line of thought pioneered by Shakura & Sunyaev (1973), let us assume that the effective viscosity in accretion disks is of hydromagnetic origin (BGH; Tout & Pringle 1992 and references therein). Alternative viscosity sources, such as thermal convection (Lin & Papaloizou 1980; Kley, Papaloizou, & Lin 1993) or gravitational instability (Paczyński 1978; Larson 1984; Laughlin & Bodenheimer 1994) will not be considered. The ultimate aim of MHD simulations then would be to obtain a self-consistent model, in which radiative energy loss is balanced by heat generation arising from orbital energy release induced by magnetic torques. At the present moment, neither computational resources nor physical understanding of the processes involved seem to be sufficient to tackle that problem; therefore, we feel that a gradual approach is more appropriate. Our strategy is to begin with simple models, allowing for selected physical processes and limited interactions between the disk and the magnetic field, and to extend them step by step toward greater complexity. Thus, the simulations presented below are not directly related to any class of real astrophysical disks. Rather, they should be regarded as laboratory experiments set up to investigate the response of magnetic fields to an environment which contains the most important ingredients of a real disk's interior.

2.1. *Numerical Methods and General Assumptions*

The simulations have been performed with the help of the two-dimensional hydrocode originally described by Różyczka (1985) and recently adapted to deal with problems of ideal MHD, following the recipes of Stone & Norman (1992). The equations solved are the continuity equation (1), the energy equation (2), the momentum and angular momentum equations (3), and the induction equations (4). The coordinates used are Eulerian cylindrical (z, r, ϕ), and rotational symmetry with respect to the axis $r = 0$ as well as mirror symmetry with respect to the plane $z = 0$ are assumed. For these coordinates and symmetries, the code successfully passed all tests suggested by Stone & Norman (1992). The basic variables are density ρ, internal energy density e, specific angular momentum J, the azimuthal component of the magnetic field B_ϕ, and velocity components v_z and v_r, together with corresponding poloidal field components B_z and B_r in the z- and r-direction, respectively. In equations (1)–(4) B_z, B_r, and B_ϕ are the components of the vector $\boldsymbol{B}$, while v_z, v_r, and J/r are represented by the vector $\boldsymbol{v}$:

$$\frac{\partial \rho}{\partial t} + \nabla \cdot (\rho \boldsymbol{v}) = 0 , \tag{1}$$

$$\frac{\partial e}{\partial t} + \nabla \cdot (e\boldsymbol{v}) = -P_g \nabla \cdot \boldsymbol{v} - \nabla \cdot \boldsymbol{F}_{\rm rad} - \hat{\boldsymbol{Q}} : \hat{\boldsymbol{E}} , \tag{2}$$

$$\rho\left[\frac{\partial \boldsymbol{v}}{\partial t} + (\boldsymbol{v} \cdot \nabla)\boldsymbol{v}\right] = -\nabla P_g - \rho \nabla \Phi + \frac{1}{4\pi}(\nabla \times \boldsymbol{B}) \times \boldsymbol{B} - \epsilon_{zr\phi}\, \mathrm{div}\, \hat{\boldsymbol{Q}} , \tag{3}$$

$$\frac{\partial \boldsymbol{B}}{\partial t} = \nabla \times (\boldsymbol{v} \times \boldsymbol{B}) , \tag{4}$$

where P_g in equations (2) and (3) is the gas pressure, related to ρ and e by the equation of state, $\hat{\boldsymbol{Q}}$ and $\hat{\boldsymbol{E}}$ are the viscous stress tensor and the symmetrized tensor of velocity derivatives, respectively, $\boldsymbol{F}_{\rm rad}$ is the radiative energy flux, and the factor $\epsilon_{zr\phi}$, which is assumed to be equal to unity in equations for v_z and v_r, and to zero in the angular momen-

tum equation (see the discussion below), has been introduced to simplify the notation.

According to the research strategy outlined above, we focus on the dynamical aspect of the disk-field and field-disk interactions, and we adopt a simplified scenario for heat generation in the disk. We confine ourselves to the framework of ideal MHD and assume that the resistivity of the medium in which the field evolves is negligibly small, i.e., that the physical dissipation of the field is negligible. Consequently, in our approach the heat generated by reconnection and/or dissipation of the field is omitted from equation (2), and the field can only affect the thermal budget of the disk through the $P_g\,dV$ work arising from motions it excites. Instead of the magnetic dissipation, we introduce an assumed α-type viscous dissipation, and we include heat gain from this effect. To satisfy these assumptions, equation (2) includes terms allowing for heat gain or loss through radiation transfer and heat gain through viscous dissipation. We assume, however, that the angular momentum redistribution arises only from magnetic torques, so that the viscous term is omitted from the angular momentum equation. This issue is further discussed in § 2.2.

The hydrodynamical part of the code is based on a second-order method with monotonicity constraints on advected quantities. The MHD part employs a descendant of the constrained transport method (Evans & Hawley 1988) to evolve the poloidal components of the magnetic field, with the original algorithm supplemented by upwinding in Alfvén wave characteristics (Stone & Norman 1992). With two exceptions the upwinding is applied to all terms in the MHD equations that describe the evolution of, or are a consequence of, magnetic fields. The exceptions are the magnetic pressure term in the momentum equations, which is treated in the same way as the gas pressure term, and the advective term in the azimuthal field equation, which is analogous to the advection terms for all scalar hydrodynamical quantities. The MHD scheme conserves the zero divergence of the magnetic field very well, but it suffers from numerical reconnection of the field on the scale of the grid spacing. While usually small in the regions of smooth flow, the latter effect becomes significant in a turbulent medium (see Hawley & Balbus 1992, and § 3.4 of the present paper). The energy of the field that has been numerically dissipated and/or reconnected is lost from the grid. The geometrical constraints disable cyclonic motions in the disk, resulting in a lack of feedback between the azimuthal and poloidal components of the field. Nevertheless, we are forced to adopt them for the simple reason that they make the problem tractable with the present-day numerical methods and resources.

2.2. *Input Physics*

The environment in which the fields evolve is an annulus of a steady state α-accretion disk orbiting a point gravity source and embedded in a uniform ambient medium. The central gravity source is assumed to be massive compared with the disk, and the self-gravity of the disk is neglected. Following Różyczka, Bodenheimer, & Bell (1994), the ambient medium and the gas within the disk are treated as separate fluids. The interface between them is defined as an equidensity surface, corresponding to the minimum density ρ_i encountered in the initial disk model. At every time step, each grid cell is labeled as belonging to the ambient medium if its density is lower than 1.01 ρ_i, and as belonging to the disk otherwise. No flow is allowed across the interface from the ambient medium into the disk, but it follows from the labeling procedure that a residual mass transfer from the disk into the ambient medium may occur. Effectively, the ambient medium serves only as a means of imposing a constant pressure boundary condition on the surface of the disk, whereby the surface itself is allowed to move almost freely across the grid. As the density of the ambient medium is reset every time step to ρ_i, the residual mass transfer from the disk into the ambient medium results in a global mass nonconservation. However, this effect is very small, and in no case was more than 1% of the mass initially contained in the grid lost by the end of a simulation. The temperature of the ambient medium ($T_{\rm amb}$) is chosen so that the ambient pressure roughly matches the lowest pressure encountered in the initial disk model. Both in the disk and in the ambient medium, the equation of state is taken to be that of an ideal gas. The ambient medium rotates around the central mass with rotational velocity equal to the local Keplerian velocity everywhere, and no other motions are allowed in it. To meet the constant pressure condition, the ambient medium is kept free of any magnetic fields by a procedure discussed in § 3.4.

The initial disk model is in thermal equilibrium, with heat sources from viscous dissipation balanced by radiative loss. The viscosity coefficient is obtained from the local values of ρ, P_g, and Ω according to the standard α-prescription

$$\eta = \frac{2}{3}\,\frac{\alpha \rho c_s^2}{\Omega}\,, \tag{5}$$

where

$$c_s^2 = \gamma\,\frac{P_g}{\rho}\,, \tag{6}$$

and $\Omega = J/r^2$ is the local angular velocity (see, for example, Ruden & Pollack 1991). Only the shear viscosity is taken into account, while the bulk viscosity coefficient is set to zero. Artificial viscosity is not applied anywhere in the disk, and the α-viscosity does not operate in the ambient medium nor in the thin layer (1–2 grid cells) immediately below the surface of the disk. To obtain the viscous heat generation rate that appears in the energy equation, all components of the viscosity tensor (Tassoul 1978) are calculated. The viscosity coefficient (eq. [5]) is used in the energy equation as well as in the r- and z-components of the momentum equation, where it is found to have a stabilizing influence on the flow. However, as we already mentioned in § 2.1, viscous torques are consistently set to zero in the angular momentum equation. We do this to avoid viscous flows of the type discovered by Różyczka et al. (1994) that could interfere with (or even quench) the flows excited by Lorentz forces. At the inner and outer radial boundary of the grid ($r = r_{\rm min}$ and $r = r_{\rm max}$, respectively) all variables are simply reset at every time step back to their initial values. This procedure in fact has very little influence on the results of the calculations, because all simulations are stopped before the magnetized region of the grid approaches the boundaries.

For the radiation transfer, Rosseland mean opacities based on solar composition are included in the manner described by Bodenheimer et al. (1990). The main sources at low temperatures (less than 3000 K) are molecules (Alexander 1975) and grains (Pollack, McKay, & Christofferson 1985). For the calculations reported in this paper, the

minimum optical depth across the grid in the z-direction is $\sim 10^2$. Most of this optical depth is associated with the disk, which is embedded in a semitransparent ambient medium ($\tau_{amb} \sim 1$). Thus, one may assume that the gas and radiation temperatures are equal everywhere, and that the radiative transfer equation may be approximated by the flux-limited radiative diffusion equation. The latter is solved by the alternating-direction implicit method described by Bodenheimer et al. (1990). The radiation transfer solver requires that the temperature at the boundary of the grid, T_b, be specified. In the ambient medium we set $T_b = T_{amb}$, whereas in the disk T_b is set equal to the local disk temperature.

2.3. *Initial Disk Model*

For the simulations presented here we employ an α-model of a protoplanetary disk around a solar-like star. However, our calculations are not meant to apply specifically to a protoplanetary disk, and there is no reason for selecting that particular model, except for the availability of detailed structural data. As we indicated at the beginning of § 2, our intention is to look for conclusions concerning the response of magnetic fields to an environment containing the most important ingredients of astrophysical disks in general (strong shear, variable gravitational acceleration and radiative energy transfer).

For the construction of the initial model, the method developed by Różyczka et al. (1994) is used. First, accurate one-dimensional vertical structure integrations for different radii between r_{min} and r_{max} are carried out for $\alpha = 0.05$, $\dot{M} = 10^{-6} M_\odot$ yr^{-1}, and a central mass of 1 $M_\odot$ (see Bell & Lin 1994 for details). The whole set of one-dimensional models is then transferred onto the two-dimensional grid by means of a linear interpolation and allowed to relax toward a stationary state without magnetic fields. During the relaxation, viscous heating and two-dimensional radiative transfer are included, but the viscous torques are omitted from the angular momentum equation. The essence of the relaxation is the damping process, in which v_r and v_z are multiplied every time step by a factor which is initially set to 0.95 and is subsequently increased up to unity. The relaxation is stopped when the total kinetic energy of z- and r-motions has stabilized. The relaxed models exhibit weak convective patterns with typical velocities of 10^{-2} km s^{-1}, much below the velocity of sound (0.3–3.0 km s^{-1}).

Two initial disk models are obtained for annuli (r_{min}, r_{max}) of (0.2, 0.5) and (1.0, 1.5) AU, hereafter referred to as the *inner disk* and the *outer disk*, respectively. The inner disk is simulated on a grid consisting of 60 × 200 points uniformly distributed in (z, r) and providing a resolution of $\approx 2 \times 10^{10}$ cm. For the outer disk, grids of 65 × 120 and 125 × 230 points are used, providing resolutions of $\approx 6 \times 10^{10}$ and $\approx 3 \times 10^{10}$ cm, respectively.

2.4. *Initial Field Generation*

In a relaxed model an initial loop of poloidal magnetic field is generated, hereafter referred to as the *seed loop*. The seed field is not generated by any realistic physical process, and both its configuration and its intensity are arbitrary. The sensitivity of simulations to the initial setup of the magnetic field is discussed in § 3.2 and 3.3. The loop-generating procedure assumes a distribution of azimuthal currents j_ϕ, for which the azimuthal component of the vector potential

$$A_\phi(x) = \int d^2x' \frac{j_\phi(x')}{|x - x'|} \tag{7}$$

is found, where x and x' are vectors in the (z, r)-plane, and it is assumed that the region with nonzero current density has a small radial extent compared to its distance from the disk center. The poloidal B-field components are then obtained from the general formula

$$B = \nabla \times A , \tag{8}$$

which, in an axially symmetric case, reduces to

$$B_z = \frac{1}{r} \frac{\partial (r A_\phi)}{\partial r} , \tag{9}$$

and

$$B_r = -\frac{\partial A_\phi}{\partial z} . \tag{10}$$

The numerically computed divergence of the poloidal field thus obtained is zero almost to machine accuracy, and it does not change noticeably during the evolution.

The seed loop is subsequently normalized to the desired field strength B_0, which we identify with the maximum field strength to be encountered in the loop. As all seed loops are flat (with a typical width-to-length ratio $\Delta z/\Delta r \sim \frac{1}{8}$; see Fig. 1*a*), B_0 is a good measure of the initial radial component B_r. We carry out simulations for seed loops with B_0 of 0.3 and 3.0 G, hereafter referred to as the *weak seed* and the *strong seed*, respectively. The weak seed loop is generated in both the inner and the outer disk, and the initial value of β (the ratio of thermal to magnetic pressure) within it approaches $\sim 3 \times 10^4$ and ~ 300, respectively. The strong seed is generated in the inner disk only, corresponding to $\beta \sim 300$. For reasons explained in § 3.1, all loops are generated above the midplane of the disk. Let us also remark that one may

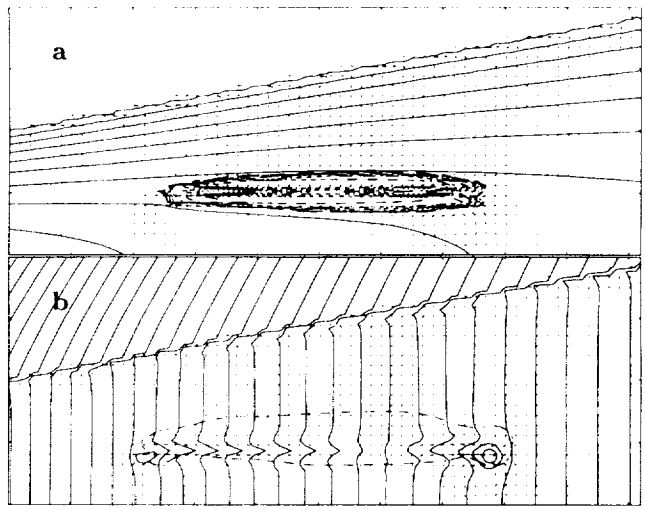

FIG. 1.—Strong seed in the inner disk shown at (*a*) $t = 0.2$ yr and (*b*) $t = 0.4$ yr. (*a*) Contours of constant density in the (r, z)-plane (*solid lines*) are separated by $\Delta \log \rho = 0.34$ with $\log \rho_{min} = -11.0$. Contours of constant β, the ratio of gas pressure to magnetic pressure (*broken lines*), are spaced logarithmically between 100 at the edge of the loop and ~ 5 inside the loop. *Arrows*: Velocity vectors with length proportional to speed and with $V_{max} = 0.15$ km s^{-1}. The horizontal feature cutting the loop into two nearly equal parts is the interface between regions with oppositely oriented azimuthal field. (*b*) Contours of constant specific angular momentum (*solid lines*) are separated by $\Delta \log J = 0.01$. *Broken line*: Contour of constant $\beta = 3000$. *Arrows*: Velocity vectors with $V_{max} = 0.26$ km s^{-1}. The distance unit on the horizontal and vertical scales is 2.76×10^{11} cm. The left and right closed J-contours correspond to a local minimum and a local maximum of J, respectively.

expect the weak seed in the outer disk and the strong seed in the inner disk to evolve similarly, because they have the same β-value. Our results reported in § 3.2 demonstrate that this is indeed the case.

The insertion of the seed field into the disk destroys the stationary equilibrium achieved as a result of the relaxation procedure. To approximately restore it, the internal energy density is adjusted locally according to

$$e = e_0 \frac{P_g}{P_g + P_m}, \tag{11}$$

where P_m is the magnetic pressure and e_0 is the original internal energy density. The relaxation procedure described in § 2.3 is then repeated, with the contribution from P_m taken into account. During the relaxation, the B-field is not allowed to evolve, i.e., all time derivatives of all B-components are set equal to zero. In general, the internal energy adjustment brought about by equation (11) brings the model so close to a stationary state that little relaxation is needed. It must be stressed here that the relaxed model with seed *is not in equilibrium* in the sense that it begins to generate the B_ϕ component as soon as the field is allowed to evolve. The aim of the somewhat tedious relaxation procedure is simply to exclude any spurious effects from artificially excited motions in the initial disk model.

3. SIMULATIONS: RESULTS

As stated in § 2.1, throughout the evolution the field is assumed to be ideally frozen into the gas, i.e., the disk gas is assumed to be perfectly conducting. Since the temperature of our initial disk models is rather low (200 K $< T <$ 2000 K), this assumption may hold only marginally, especially in the outer disk (see Fig. 1*a* of Stepinski, Reyes-Ruiz, & Vanhala 1993). The neglect of the finite resistivity of the disk medium comes partly from our research strategy and partly from the conviction that, at the modest resolution provided by our grids, the effects of physical and numerical diffusion would be difficult to separate. However, the finite resistivity of the disk medium should definitely be taken into account in future experiments.

3.1. *Early Evolution*

In all cases, the early evolution of a seed loop inserted into an accretion disk follows the same general track. In the first phase (*the buildup phase*), the B_ϕ component is generated by shear at a rate nearly constant in time and approximately given by

$$\frac{dB_\phi}{dt} \approx -\frac{3}{2}\Omega B_r . \tag{12}$$

The growth of B_ϕ in the buildup phase of the weak seed in the inner disk is illustrated in Figure 2, where the maximum azimuthal field B_ϕ^m found in the grid is plotted against time, together with predictions based on equation (12). For a given time, the predicted value of the azimuthal field is obtained from the momentary maximum value of the radial component B_r^m found in the grid and from Ω corresponding to the momentary location of B_r^m. The two sets of data are in good agreement, demonstrating that the resolution we are able to achieve within the seed loop is sufficient to properly describe the linear evolution of the field. For $t > 1$ yr, the effects of motions within the seed and the effects of the overall expansion of the seed become visible, and the maximum B_ϕ in the grid falls below the value calculated from equation (12). At the end of the buildup phase, loss of field owing to numerical reconnection also becomes noticeable (see discussion in § 3.4).

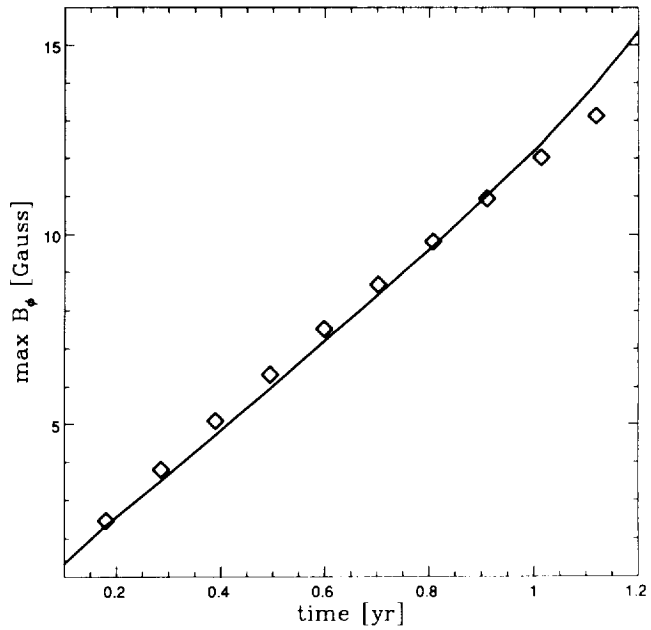

FIG. 2.—Growth of the azimuthal field in the buildup evolutionary phase of the weak seed in the inner disk. *Diamonds*: Maximum B_ϕ value found in the grid at a given time. *Curve*: B_ϕ value calculated for that time from the linear formula (eq. [12]).

Let us note in passing that, according to equation (12), the sign of B_ϕ is determined by the sign of B_r, which means that the azimuthal field in the upper half of the loop is directed oppositely to the azimuthal field in the lower part of the loop. The fact that B_ϕ reverses its polarity inside the loop motivated us to insert the seed loops away from the midplane of the disk, so that the oppositely oriented field patches would form in the grid, and the interaction between them could be taken into account in our simulations.

As soon as the azimuthal field appears in the disk, a magnetic torque, corresponding to the azimuthal component of the Lorentz force

$$L_\phi \approx \frac{1}{4\pi} B_r \frac{1}{r}\frac{\partial}{\partial r} r B_\phi , \tag{13}$$

begins to act on the disk gas. Let us stress again that the last two equations are approximate and they become invalid when B_z and/or vertical gradients of B_ϕ and Ω cannot be neglected. The Lorentz force L_ϕ is *negative* at the inner edge of the loop and *positive* at the outer edge, where *inner* and *outer* identify the location of the loop's edge with respect to the disk center. As a result, the torque associated with L_ϕ causes the angular momentum to drift from the inner into the outer edge of the loop. In response, the loop stretches radially (both inward and outward) while essentially maintaining its vertical extent (Fig. 1). It is worth stressing that angular momentum redistribution in the loop results in a net flow of mass toward the center of the disk, associated with an orbital energy release, and that the orbital energy of the disk is mainly transformed into the energy of the azimuthal field. The radial expansion of the loop is a manifestation of the magnetorotational instability discussed by

BGH. However, because we use different initial and boundary conditions, our results cannot be directly compared to theirs. The one exception is the circular poloidal loop described by Hawley & Balbus (1991) in their § 3.5 and illustrated in their Figure 9. Indeed, in that case the loop evolves mainly by radial stretching, just as our loops do throughout the buildup phase.

According to equation (13), the evolution of the disk should not depend on the orientation of the field in the seed loop, i.e., two seed loops differing only in the orientation of the initial field should undergo the same evolutionary changes. To check the consistency of the MHD code, the calculation illustrated in Figure 1 was repeated with the direction of the initial field reversed. No differences were found.

3.2. *Buoyant Phase*

Eventually, because of continuous B_ϕ growth, the value of β inside the magnetized region approaches unity, and at the upper surface of the loop a clear wavy pattern appears. At this moment the loop enters the *buoyant* evolutionary phase, in which plumes of magnetized gas begin to rise toward the surface of the disk. We tested the credibility of our simulations in that phase by following the evolution of a weak seed in the outer disk at resolutions of 6×10^{10} and 3×10^{10} cm. We find that throughout both the buildup phase and the early stages of the buoyant phase the results are hardly distinguishable. The high- and standard-resolution models begin to differ only at more advanced stages of the buoyant phase (Fig. 3), when the plumes arrive at the surface of the disk. However, even then the differences are insignificant as far as the global parameters of the model (flow pattern, total magnetic energy, and total kinetic energy of meridional motions) are concerned. The basic conclusion from this experiment is that our standard grids are able to resolve the effective radial wavelength λ_b of the buoyant instability.

In Figure 4 different seeds evolving in the inner disk are compared at the moment when the first buoyant plume reaches the surface of the disk. Figure 4*a* shows the standard strong seed (cf. Fig. 1), originally extending over $\Delta r = 1.54 \times 10^{12}$ cm, whose center is located at $z_0 = 2.8 \times 10^{11}$ cm above the midplane of the disk and $r_0 = 5.46 \times 10^{12}$ cm from the rotational axis. The standard weak seed with the same original dimensions and location is shown in Figure 4*b*. Figure 4*c* shows a weak seed with standard z_0 and r_0 but extending over $\Delta r = 2.5 \times 10^{12}$ cm, whereas a weak seed with the standard r_0 and Δr but originally located at $z_0 = 3.47 \times 10^{11}$ cm is illustrated in Figure 4*d*. The simulations demonstrate that λ_b is a function of both the seed strength and the location of the unstable magnetized area in the disk. It can be seen that at a given r_0, λ_b grows larger with increasing seed strength B_0 (compare Figs. 4*a* and 4*b*), increasing distance r from the disk center (inspect Fig. 4*b* or 4*c*) or decreasing distance z from the midplane of the disk (compare Figs. 4*b* and 4*d*). The first effect is very clear, while the remaining two are only detectable after a closer inspection of Figure 4. It may also be noted that λ_b in the outer disk is much longer than any of the wavelengths excited in the inner disk.

The excitation mechanism of the buoyant instability will be discussed in § 3.5. Here we would like to point out another important property of magnetic buoyancy, namely, that radiative energy transfer has a significant effect on its

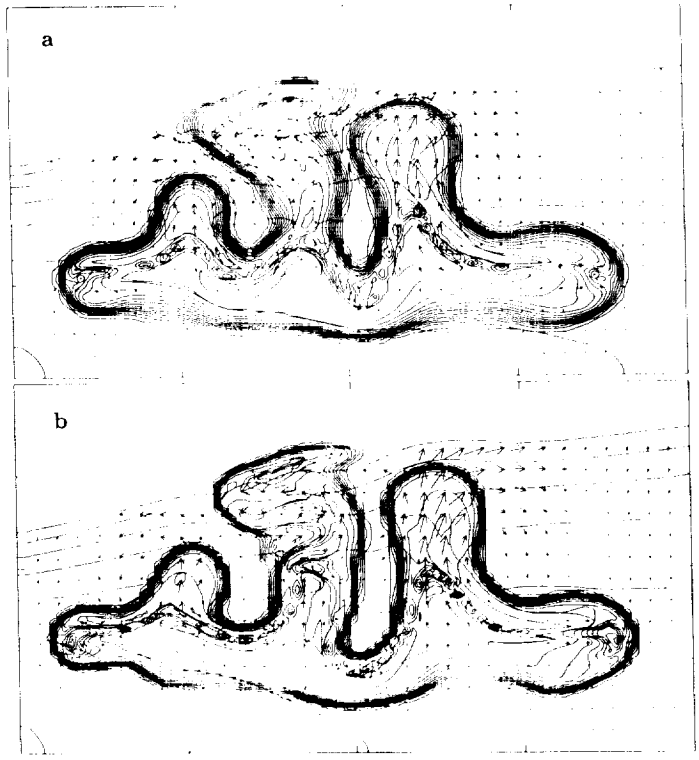

FIG. 3.—Weak seed in the outer disk shown at the end of the buoyant phase ($t = 4.55$ yr). (*a*) Standard resolution: $\Delta z = \Delta r = 6 \times 10^{10}$ cm. (*b*) High resolution: $\Delta z = \Delta r = 3 \times 10^{10}$ cm. Contours of constant density in the (r, z)-plane (*almost horizontal, widely spaced lines*) are separated by $\Delta \log \rho = 0.25$ with $\log \rho_{\min} = -11.25$. Contours of constant magnetic pressure (*closely spaced and irregular lines*) are separated by $\Delta \log P_m = 0.3$ with $(\log P_m)_{\min} = -3.9$. *Arrows*: Velocity vectors with $V_{\max} = 0.5$ km s^{-1}. The distance units on the horizontal and vertical axes are 1.84×10^{12} and 10^{12} cm, respectively.

efficiency. It has been recognized for a long time that the magnetic buoyancy is aided by radiative heat flow into the rising elements. To explain this effect let us note that in the absence of radiative energy transfer the elements would cool adiabatically, thus weakening the effective Archimedes force (see Parker 1975; Stella & Rosner 1984). Here we are able to demonstrate this effect by comparing two simulations of the strong seed in the inner disk (Fig. 5). With all initial and boundary conditions identical, one of the simulations allows for the radiative transfer (Fig. 5*a*), while in the other the radiative transfer and the viscous heat generation are both shut off (Fig. 5*b*). In the nonradiative case, the buoyant plumes indeed grow much more slowly (while the wavelength of the buoyant instability does not seem to be affected to any significant degree). Unfortunately, because of the limited resolution of our calculations we are not able to quantify this effect. The calculations illustrate the important point that magnetic buoyancy differs fundamentally from thermal convection, in which the effect of radiation is to cool the rising elements and reduce the convective flux.

3.3. *Saturation Phase*

At the end of the buoyant phase the disk undergoes a rather rapid transition to a state in which the initial, ordered field structure has evolved into a chaotic ensemble of patches (Fig. 6). However, while the patches are well defined and separated by field-free regions in the weak-seed case, in the strong-seed case they are diffuse, and the gas

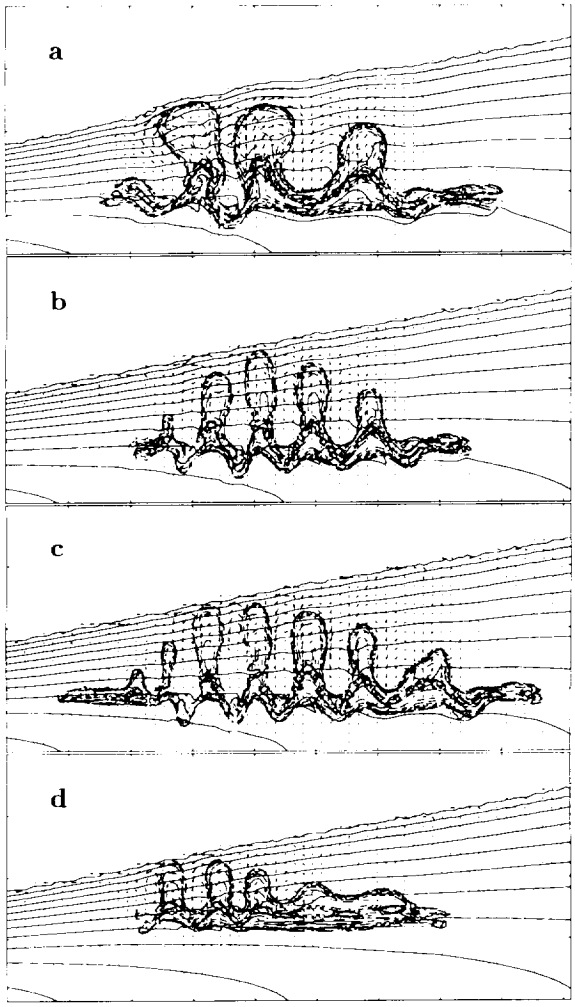

FIG. 4.—Four different seeds in the inner disk are compared at an advanced stage of the buoyant phase (at the moment when the most evolved buoyant plume arrives at the surface of the disk). (*a*) Strong seed. (*b–d*) Weak seeds. Contours of constant density in the (*r*, *z*)-plane (*solid curves*) are shown with $\Delta \log \rho = 0.28$ and $\log \rho_{min} = -11.0$ in all frames. Contours of constant β with logarithmic spacing (*broken curves*) have $\log \beta_{min} = 0.09$, 0.45, 0.35, and 0.38 in (*a–d*), respectively, $\log \beta_{max} = 1.5$ in (*a*), and $\log \beta_{max} = 1.8$ in (*b–d*). *Arrows*: Velocity vectors with $V_{max} = 1.30$, 0.23, 0.18, and 0.23 km s^{-1} in (*a–d*), respectively. Evolutionary times: 0.84, 4.15, 4.32, and 2.22 yr in (*a–d*), respectively. The distance unit on the horizontal and vertical scales is 3.08×10^{11} cm.

between them is weakly magnetized. Further, in the strong-seed case the average saturation value of β is close to unity, whereas in the weak-seed case it stays greater than five. In the strong-seed case the total magnetized area is larger, so that the difference in saturation values of the total field energy between the two cases approaches an order of magnitude. We conclude that at least up to evolutionary times indicated in Figure 6 the disk is able to preserve the memory of initial conditions. The explanation as to why the final total field energies are different is deferred to the end of § 3.5. The disk states shown in Figure 6 are the final ones we were able to achieve. The simulations had to be stopped here because of uncontrolled field creation and annihilation on the grid-spacing scale.

3.4. *Energetics*

The monitoring of various forms of energy contained in the disk leads to further clarification of the physical processes responsible for the evolutionary changes described in §§ 3.1–3.3. As mentioned in § 3.1, in the buildup phase the azimuthal field grows at the expense of the orbital energy of the gas, which is driven by magnetic torques toward the center of the disk. At the same time, the poloidal field slowly decays as a result of numerical diffusion and/or reconnection, and its energy E_p decreases (Fig. 7). Thus, the total energy of the field E_t quickly becomes dominated by the energy of the azimuthal component, and, in accordance with equation (12), it grows roughly proportionally to t^2. The accompanying growth of the kinetic energy K associated with the motions in the meridional plane results mainly from the radial expansion of the seed loop.

The total energy of the field keeps growing as $\sim t^2$ until the numerical loss of B_ϕ becomes significant. In the buildup phase, the only factor responsible for that loss is the auto-

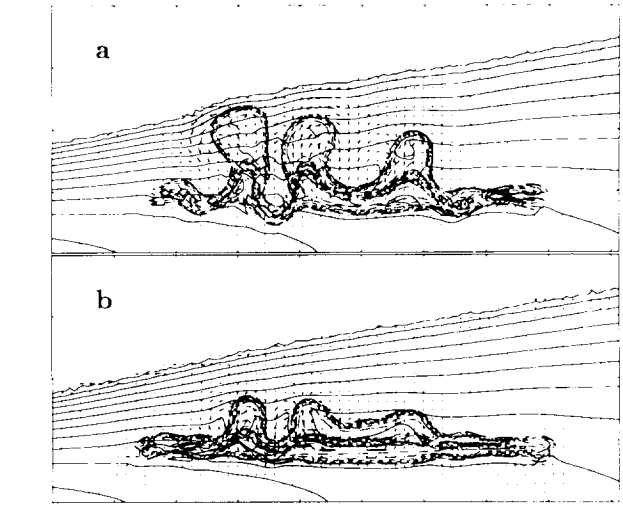

FIG. 5.—Strong seeds evolving in the inner disk (*a*) with radiation transport and (*b*) adiabatically are compared at $t = 0.82$ yr. Curves, arrows, $\Delta \log \rho$, and $\log \rho_{min}$ are the same as in Fig. 4. (*a*) and (*b*) $\log \beta_{min} = -0.14$ and -0.38, respectively; $\log \beta_{max} = 1.5$ in both frames. (*a*) and (*b*) $V_{max} = 1.28$ and 0.53 km^{-1}, respectively. Distance unit: 3.08×10^{11} cm.

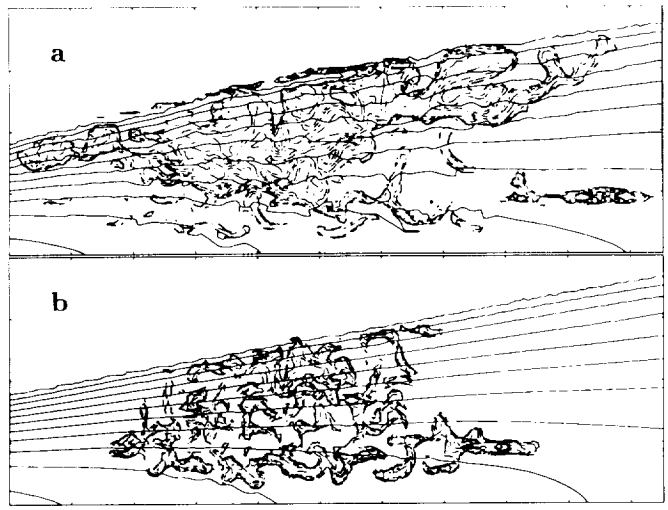

FIG. 6.—The final calculated states of (*a*) strong and (*b*) weak seed evolving in the inner disk. Evolutionary times: (*a*) 4.90 yr and (*b*) 11.90 yr. Curves, $\Delta \log \rho$, and $\log \rho_{min}$ are the same as in Fig. 4. In frames (*a*) and (*b*) $\log \beta_{min} = -0.09$ and 0.74, $\log \beta_{max} = 1.0$ and 2.0, respectively. Distance unit: 3.08×10^{11} cm.

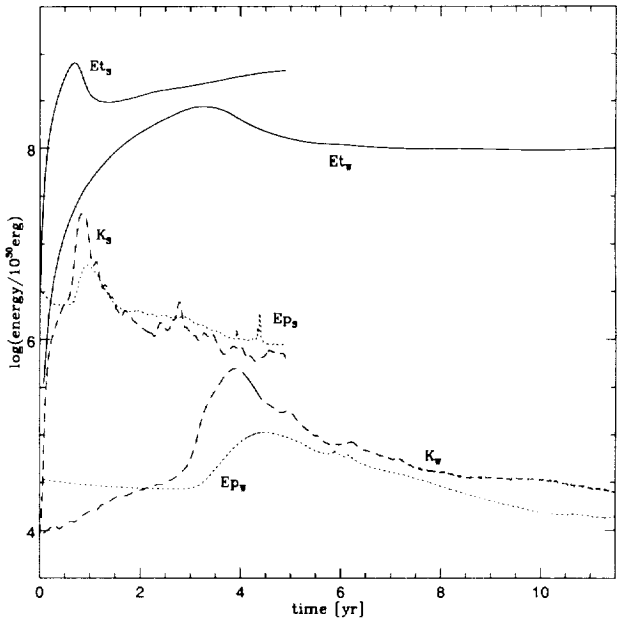

FIG. 7.—Total magnetic energy (E_t), total energy of the poloidal field (E_p), and total kinetic energy of motions in the meridional plane (K) as a function of time for the strong (subscript s) and weak (subscript w) seeds evolving in the inner disk.

matic annihilation (reconnection) of oppositely oriented fluxes on the grid-spacing scale, which occurs whenever oppositely oriented patches of B_ϕ field are advected into the same grid cell. In the early buildup phase, the interface dividing the seed loop into two halves with opposite signs of B_ϕ stays flat and smooth (Fig. 1*a*), there is little motion across it, and the annihilation rate is a small fraction of the generation rate. Only in the buoyant phase does the numerical reconnection become important enough to slow the growth of E_t. The primary cause of the increased numerical reconnection is vigorous buoyant flow, which causes the interface between the areas of oppositely oriented B_ϕ to bend sharply, while the velocities perpendicular to it grow up to $\sim 0.02 c_s$ in the weak seed case (Fig. 4*b*) and $\sim 0.1 c_s$ in the strong seed case (Fig. 4*a*). The buoyant flow also causes the total area of the deformed loop to increase rapidly. As a result, the intensity of the azimuthal field decreases, owing to geometrical dilution of the azimuthal flux. This effect is probably more important than the numerical effect until the latest stages of the evolution.

In the strong field case, the numerical loss and the geometrical dilution of B_ϕ acting together cause E_t to drop by half an order of magnitude in less than ~ 0.5 yr between ~ 0.75 and ~ 1.25 yr from the beginning of the simulation. The same effect is much gentler in the weak seed case, where E_t decreases by a somewhat smaller amount between ~ 3.5 and ~ 5.5 yr from the beginning of simulation (Fig. 7). In both cases, the poloidal energy E_p reverses its downward trend and starts to increase during the epoch of declining E_t, whereas the kinetic energy K markedly accelerates its growth before reaching a maximum value. As we already stressed in §§ 2.1 and 2.4, the null divergence of the poloidal field is always satisfied in our calculations (i.e., the total poloidal flux stays constant), which means that the observed increase of the poloidal field energy does not violate the axisymmetric antidynamo theorem (see, e.g., Parker 1979, § 18). E_p grows simply because the poloidal field lines are wound more tightly; following the picturesque terminology of Hawley & Balbus (1992), we may say that the magnetized gas is *kneaded* by buoyancy-induced flows, with progressively smaller structures appearing in it as time goes on. It is worth noticing that both K and E_p increase at the expense of the azimuthal field energy, which is first transformed into the kinetic energy of buoyant motions and then into the poloidal field energy as a result of the kneading phenomenon.

At the moment the first plume arrives at the surface of the disk another sink of magnetic energy opens, originating from our condition of constant ambient pressure (§ 2.2). Any azimuthal field advected into the ambient medium by the residual mass transfer from the disk into the ambient medium is assumed to annihilate on the spot, and it is simply removed from the grid. Any poloidal field is prevented from extending into the ambient medium through a procedure in which the electromotive force (hereafter emf) in the induction equation is gradually reduced from its exact value just below the surface to zero in the ambient medium (note that, in the constrained transport method, the modifications of emf do not violate the poloidal flux conservation condition). On the average, the surface loss of the azimuthal field is small (less than 1%) compared to the loss from numerical reconnection in the disk. Occasionally, however, it can exceed the latter because of a burstlike escape of B_ϕ into the ambient medium. The influence of emf reduction on the poloidal field evolution is also small as far as the total energy of the poloidal field is concerned; we checked that the E_p curves obtained with and without reduction of the emf never differ by more than $\sim 10\%$. However, this procedure has a significant stabilizing effect on the evolution: if the emf is not reduced, the vigorous kneading just below the surface of the disk quickly brings the code to its limits. As far as the numerical reconnection is concerned, the extent to which it mimics real physical reconnection is difficult to estimate, since the true reconnection rate depends on the detailed geometry of the field, which is not known. This question is important, and it will be considered in the future.

The epoch of E_t decline comes to an end when a near equilibrium between field generation and destruction is reached in the saturation phase. B_ϕ is now generated from shearing of a highly nonuniform poloidal field which spreads over a larger and larger area of the disk. There is no well-defined interface separating regions with oppositely oriented B_ϕ, the motions are chaotic, and azimuthal field patches with different signs annihilate "on the spot," at almost the same rate at which they are created, i.e., on a timescale of several orbital periods. It may be noted that this timescale is longer than the shortest possible timescale for physical reconnection of a field composed of thin patches, the latter being comparable to the orbital period (Różyczka, Turner, & Bodenheimer 1995). As a result, the average intensity of the azimuthal field remains nearly constant, and the observed slow increase of E_t is almost entirely caused by the increase of the total magnetized area. With the characteristic scale of magnetic field structure approaching the grid resolution, the numerical reconnection and/or diffusion of the poloidal field also become more and more effective. As a result, in the saturation phase E_p decreases slowly, with occasional short-term bursts owing to locally enhanced kneading. The fact that the kinetic energy of meridional motions also declines in the saturation

phase is a bit more difficult to explain. In order to elucidate this issue, let us recall that the increase of K at the end of the buoyant phase was mainly caused by energy injection on large scales (comparable to the characteristic size of the first strong buoyant plumes). Because the magnetic field has become more homogeneous, that process is much less effective now (i.e., there is much less buoyant stirring on large scales), while on small scales K is partly converted into E_p and partly dissipated by viscosity (see § 2.2) at about the same rate as before.

3.5. *Excitation Mechanism of the Buoyant Instability*

The initial conditions for our simulations are too complicated for a detailed linear stability analysis. However, even an approximate analysis based on a "submerged sharp boundary" case discussed by Parker (1979, p. 316) may be useful. To apply it, we will have to adopt two simplifying assumptions. First, we follow Parker by adopting the Boussinesq approximation, in which the effect of compressibility is neglected for the perturbed quantities. Second, we assume that the upper boundary of the magnetized region is originally entirely flat and infinite in extent (i.e., that the curvature of the initial poloidal field lines is unimportant), and that the generated azimuthal component is equivalent to a uniform field with straight lines perpendicular to the initial poloidal field lines. We shall also assume that the gravitational acceleration and total (gas plus magnetic) pressure are uniform in the vicinity of the upper boundary of the magnetized region. The stable lower boundary of the magnetized region will be entirely excluded from our considerations.

To facilitate referencing to Parker's work, let us adopt the same Cartesian coordinate system (x, y, z), and let us use the same symbols. Let the y-axis point in our azimuthal direction, while x- and z-axes will point in our radial and vertical directions, respectively. Further, let the gravitational acceleration g be oriented toward the midplane of the disk (i.e., in the negative z-direction). For the present analysis, we locate the interface between magnetized and field-free regions at $z = 0$. The magnetic field is perpendicular to g and confined to the half space $z < 0$, hereafter referred to as domain 1 (the field-free region is referred to as domain 2). Although the total pressure is continuous across the interface, the density in domain 2 is larger than that in domain 1 by an amount $\Delta\rho$ because of the drop in magnetic pressure. Neglecting changes in the sound speed c_s, the total pressure

$$p_t = \rho c_s^2 + (B_x^2 + B_y^2)/8\pi \tag{14}$$

in domain 1 maintains a balance with that in domain 2 when

$$\Delta\rho = (B_x^2 + B_y^2)/8\pi c_s^2 , \tag{15}$$

where B_x (our B_r) is approximately constant in time and B_y (our B_ϕ) grows in time according to equation (12).

Our first assumption results in

$$\nabla \cdot \boldsymbol{v} = 0 , \tag{16}$$

where $\boldsymbol{v}$ is the perturbed velocity. The rotational part of $\boldsymbol{v}$ only contributes to oscillatory Alfvén waves and therefore is irrelevant here. In domain 1, the irrotational part of $\boldsymbol{v}$ may be expressed in terms of a potential function

$$\boldsymbol{v} = -\nabla\Psi , \tag{17}$$

with

$$\Psi = C(t) \exp (ixk_x + iyk_y + z\sqrt{k_x^2 + k_y^2}) , \tag{18}$$

where $C(t)$ is a function of t, k_x, k_y, and k_z are components of the wavevector $\boldsymbol{k}$, and i is the imaginary unit. From the induction equation (4) we find the perturbed field components

$$b_x = (B_y k_x k_y + B_x k_x^2)\mathscr{C}\Psi ,$$

$$b_y = (B_y k_y^2 + B_x k_x k_y)\mathscr{C}\Psi , \tag{19}$$

$$b_z = (-iB_y k_y\sqrt{k_x^2 + k_y^2} - iB_x k_x\sqrt{k_x^2 + k_y^2})\mathscr{C}\Psi , \tag{20}$$

where $\mathscr{C} = \int_0^t C(t')dt'$. For domain 2, the potential function for the perturbed velocity is

$$\Phi = S(t) \exp (ixk_x + iyk_y - z\sqrt{k_x^2 + k_y^2}) . \tag{21}$$

The sign for the z dependence of the potential functions is chosen such that Ψ and Φ vanish as z approaches $-\infty$ and $+\infty$, respectively. The location of the perturbed interface is given by a Lagrangian variable $\xi(x, y, t) = \int v_z dt$. The requirement for v_z to be continuous across the interface implies that

$$C(t) + S(t) = 0 \tag{22}$$

at $z = \xi$. Remembering that in domains 1 and 2 the pressure at the perturbed interface is lower than that at $z = 0$ by $g\rho\xi$ and $g(\rho + \Delta\rho)\xi$, respectively, we can obtain from equation (3) the following condition for pressure balance at the interface (see also Parker 1979, p. 318):

$$(\delta p_2)_0 = (\delta p_1)_0 + \frac{B_y}{4\pi}(b_y)_0 + \frac{B_x}{4\pi}(b_x)_0 + g\,\Delta\rho\xi + \Delta Q_{zz} , \tag{23}$$

where δp is the pressure perturbation, subscripts 1 and 2 refer to perturbations in magnetized and nonmagnetized domains, respectively, and subscript 0 denotes a value calculated at $z = 0$. The last term in equation (23) accounts for the nonvanishing difference in the zz component of the viscous stress tensor across the interface:

$$\Delta Q_{zz} = \rho\nu\left(\frac{\partial v_z}{\partial z}\right)_1 - (\rho + \Delta\rho)\nu\left(\frac{\partial v_z}{\partial z}\right)_2$$

$$= (2\rho + \Delta\rho)\nu(k_x^2 + k_y^2)\Psi , \tag{24}$$

where $\nu = \eta/\rho$ and η is given by equation (5). After appropriate substitutions, equation (23) yields the amplitude equation

$$(2\rho + \Delta\rho)\left[\frac{\partial\Psi}{\partial t} + \nu(k_x^2 + k_y^2)\Psi\right]$$

$$-\left[g\,\Delta\rho\sqrt{k_x^2 + k_y^2} - \frac{(B_y k_x + B_x k_y)^2}{4\pi}\right]\int_0^t \Psi\, dt' = 0 . \tag{25}$$

Since our numerical models are axisymmetric, in the following, let us focus on modes with $k_y = 0$ which do not bend the lines of B_y (i.e., our azimuthal field). We shall refer to them simply as *interchange modes*, keeping in mind, however, that only the azimuthal field lines are subject to pure interchange modes, while poloidal field lines may

still undulate. Under the substitutions $\tau = \Omega t$, $k = Hk_x$, $g = \Omega^2 H$, and $c_s = \bar{c}_s \Omega H$ (where H is the disk half-thickness and ΩH is the midplane value of the sound speed as given by the standard theory of thin accretion disks), equation (25) reduces to

$$\frac{dC(\tau)}{d\tau} + \frac{2\bar{c}_s^2 \alpha k^2 C(\tau)}{3} + \left[\frac{2k^2 - k(1 + 9\tau^2/4)}{2\beta_0 + 1 + 9\tau^2/4}\right] \int_0^\tau C(\tau')d\tau' = 0 , \tag{26}$$

where β_0 is the initial value of β.

The linear integrodifferential equation (26) for the amplitude C was solved numerically as an initial value problem with the help of a fourth-order Runge-Kutta method. To account for the displacement of the interface (i.e., the upper surface of the loop) from the midplane of the disk $\bar{c}_s^2$ was set equal to 0.5. The results of integrations for $\alpha = 0.05$ and $\alpha = 0.01$ are plotted in Figure 8 as a function of k and τ, with C normalized to unity at $\tau = 0$ for all k. In each panel the curves are separated by equal intervals of time ($\Delta\tau = 3$ and 10 for strong and weak seed models, respectively). The highlighted curves in the $\alpha = 0.05$ panels correspond to the beginning of the buoyant phase as determined from our simulations (epoch $\tau = 15$ for the strong seed and $\tau = 80$ for the weak seed). Note that, at these epochs, maximum C is attained for $k \sim 5$–6, which agrees reasonably well with the wavelengths actually excited (Figs. 3 and 4).

Figure 8 also indicates that short-wavelength modes grow at a significantly lower rate than the most unstable mode. This finding runs contrary to the original results of Parker, according to which, in the submerged sharp boundary case, shorter wavelengths have consistently higher growth rates. This difference is a result of the presence of both the poloidal field and the viscosity (factors which were absent from Parker's analysis). In equation (26), the viscous (i.e., the second) term clearly damps the growth of perturbed quantities. The effectiveness of the viscous damping may be estimated with the help of the dimensionless damping timescale

$$\tau_d = \frac{3}{2\bar{c}_s^2 \alpha k^2} . \tag{27}$$

In our numerical simulations, τ_d approaches unity (i.e., the dynamical timescale) for wavelengths comparable to H, while perturbations with $\lambda < H$ are damped on timescales shorter than the dynamical timescale. A similar stabilizing role is played by the tension of the B_x (our B_r) lines. In order to elucidate this effect, let us set $\nu = 0$ and define a characteristic timescale of the amplitude growth

$$\tau_g = \frac{C}{dC/d\tau} . \tag{28}$$

Despite the fact that τ_g decreases with τ initially and

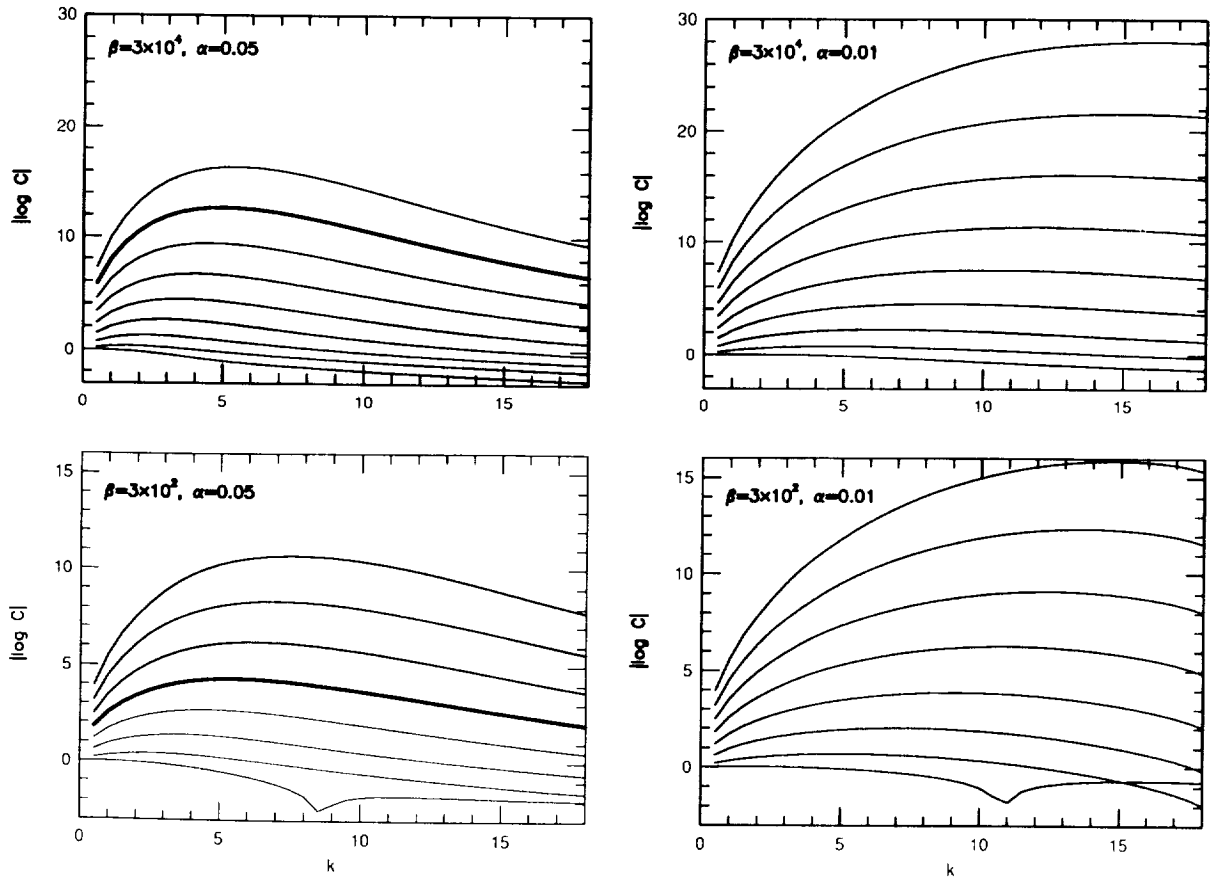

FIG. 8.—Results from linear stability analysis. The amplitude of the perturbation is plotted as a function of wavenumber $k = 2\pi H/\lambda$ at several evolutionary times, where H is the half-thickness of the disk. Each frame is labeled with the assumed initial ratio (β) of gas pressure to magnetic pressure and with the viscosity parameter (α). The times for the cases $\beta = 3 \times 10^2$ start at $\Omega t = 3$ (*lowest curves*) and increase upward in increments of $\Omega t = 3$. The times for the cases $\beta = 3 \times 10^4$ start at $\Omega t = 10$ (*lowest curves*) and increase upward in increments of $\Omega t = 10$. *Heavy lines*: time of onset of instability in the numerical simulations.

approaches a constant for large τ, let us approximate

$$\tau_g \approx \frac{1}{C(\tau)} \int_0^\tau C(\tau')d\tau' . \quad (29)$$

Based on this approximation, equation (26) reduces to

$$\frac{1}{\tau_g} + \frac{2k^2 - k(1 + 9\tau^2/4)}{2\beta_0 + 1 + 9\tau^2/4} \tau_g = 0 , \quad (30)$$

yielding the following stability condition in the absence of viscosity:

$$k > \frac{1}{2}\left(1 + \frac{9}{4}\tau^2\right) \approx \tau^2 . \quad (31)$$

A comparison of the corresponding left and right panels in Figure 8 shows that for the parameters considered here, the viscous effects on the stability of the buoyant modes may dominate those resulting from the tension of B_r lines. This result, however, is not absolutely certain. Also, the dependence of the most unstable wavelength on the initial seed strength, clearly visible in the simulations, is detected only marginally by the linear stability analysis (compare the two left panels with $\alpha = 0.05$ in Fig. 8). These two facts indicate that additional calculations and a more detailed analysis would be necessary to clearly assess the role of both factors. However, such an analysis is unlikely to change the main conclusion of the present section: the plumes observed in our simulations originate from interchange modes acting predominantly on the azimuthal field, and mediated by the presence of the poloidal field and nonnegligible viscosity. Moreover, in accordance with the simulations, the present analysis predicts that the most unstable wavelength should scale with the half-thickness of the disk. Based on this analysis, we can also provide an explanation for the difference in the final total field energies mentioned in § 3.3. Measuring the logarithmic derivative of the perturbation amplitude $d \ln C/d\tau$, we find that it first approaches unity at the peak of the highlighted curves in the left panels of Figure 8. The corresponding timescale for amplitude growth τ_g also approaches unity, which means that the perturbations begin to grow on a dynamical timescale, and a transition from the buildup to the buoyant phase is initialized. At the moment when τ_g drops to unity, β predicted by the linear analysis approaches ~ 0.6 and ~ 2.1 for the strong and weak seed, respectively. Shortly afterward, strong buoyant motions begin to stir the disk, and the reconnection rate goes up, preventing further growth of B_ϕ. Thus, the field saturates at a strength not much different from the one it had when τ_g approached unity for the fastest growing mode.

4. SUMMARY AND DISCUSSION

The simulations reported in the preceding sections followed the evolution of a seed poloidal field in an axisymmetric accretion disk. We found that the azimuthal component of the field B_ϕ grows as a result of shear until the thermal equipartition value of $\beta = 1$ is approached. At the same time, the seed spreads radially (toward both the center of the disk and its outer edge) as a result of the magneto-rotational instability (hereafter MRI). Within the seed, the angular momentum of the disk gas is removed by magnetic torques from mass elements at smaller orbital radii, and it is added to mass elements at larger orbital radii. The growth of B_ϕ is stopped by vigorous buoyant motions leading eventually to partial ejection of the field from the disk, fragmentation of the seed, and the establishment of a turbulent velocity field. The linear stability analysis indicates that the buoyancy effects are a result of interchange modes of the Parker instability (Parker 1979, § 13) acting on the azimuthal component of the field, with the effectively excited wavelength depending on the poloidal seed strength and the effective viscosity assumed for the disk gas. At later evolutionary times, a quasi-stationary state is reached, in which the total magnetic energy of the disk slowly grows because of radial expansion of the magnetized region, while the average values of field components either remain roughly constant or decrease slowly owing to numerical reconnection. In that state, the poloidal field assumes a patchy structure, with the medium between patches being either field-free or more weakly magnetized than the patches themselves. (Let us note that a patch of the poloidal field, for example, one of those plotted in Fig. 6*b*, is also a meridional cross section of a bundle of toroidal field lines).

In our models, both the field intensity at which buoyancy begins to effectively operate and the saturation intensity decrease with decreasing initial seed field strength. The dependence, however, is rather weak (see § 3.3). One may safely assume that in the presence of $B_\phi \rightarrow B_r$ feedback the seed fields would be amplified, and it is likely that a saturation intensity independent of the initial seed strength (i.e., defined solely by the disk's microphysics) would be achieved. Unless the three-dimensional effects or physical dissipation of magnetic fields prove to be very important, on the basis of our simulations, it is rather difficult to imagine that the field would saturate at $\beta \gg 1$. Thus, at least in the realm of ideal MHD, we expect the buoyant dynamo to generate rather strong fields. On the other hand, our calculations indicate that $\beta = 1$ is an absolute limit to field amplification, since already at $\beta \approx 1$ buoyant motions are so vigorous that the field begins to escape from the disk. The same limiting field strength was obtained by Galeyev et al. (1979), who discussed a classical turbulent disk dynamo. Let us note that at $\beta \approx 1$ the Alfvén velocity, which may be regarded as a reasonable approximation to the buoyancy-generated velocities (Meyer & Meyer-Hofmeister 1983; Tout & Pringle 1995), is comparable to the velocity of sound c_s. The characteristic timescale for the field escape is then only $H/c_s \approx 1/\Omega$.

From our numerical results we can now estimate the effective viscosity parameter α introduced by Shakura & Sunyaev (1973). For simplicity, we shall assume that in the saturation state the field is indeed collected in rather well-defined patches (see Fig. 6*b*), and that each patch evolves in the same way as the initial seed loop, experiencing its own buildup phase (however, with a value of B_r which does not necessarily have to be the same as that of the initial seed). We further assume that the buildup phase always ends at $\beta = 1$, neglecting the weak dependence of saturation intensity on B_r. In other words, we assume that the field saturates when the magnetic pressure generated by the azimuthal component of the field becomes equal to the thermal pressure. If the initial β of a typical patch is significantly smaller than unity, and if B_r stays roughly constant throughout the buildup phase, then it follows from equation (12) that the time t_b needed to make the azimuthal field effectively buoyant, i.e., to achieve the saturation value of

$$B_\phi = c_s\sqrt{8\pi\rho} , \quad (32)$$

is given by

$$t_b = \frac{2}{3}\frac{c_s}{\Omega B_r}\sqrt{8\pi\rho}\,. \tag{33}$$

During that time the accumulated magnetic torque per unit mass results in a specific angular momentum change of

$$\Delta J = \frac{4}{3}\frac{c_s^2}{\Omega}\,, \tag{34}$$

resulting in an average magnetic torque

$$\dot{J}_m = \frac{\Delta J}{t_b} = \frac{2c_s^2}{\sqrt{\beta_r}}\,, \tag{35}$$

where

$$\beta_r = \frac{8\pi\rho c_s^2}{B_r^2}\,. \tag{36}$$

Comparing $\dot{J}_m$ with the viscous "α-torque,"

$$\dot{J}_v = \frac{3}{2}\alpha c_s^2\,, \tag{37}$$

we get

$$\alpha = \frac{4}{3}\frac{1}{\sqrt{\beta_r}}\,. \tag{38}$$

Setting $\beta_r = \beta_0$ in order to apply this general formula to our original strong and weak seed fields, we obtain an effective α of 0.06 and 0.006, respectively. We see that in the strong field case a (coincidental) agreement is found between the assumed and the effectively generated value of α. In two-dimensional calculations, the same α-values are applicable during the saturation stage, because B_r approximately preserves its initial value. However, in three-dimensional calculations B_r would be expected to increase, resulting in an increase in the effective value of α during the evolution.

The enforced axial symmetry of our simulations prevents the transformation of B_ϕ into the poloidal components B_z and B_r. However, in three dimensions such a transformation is unavoidable, since the Coriolis force acting on buoyant elements results in helical twisting of the azimuthal field lines. The feedback between B_ϕ and B_r is a necessary requirement for the dynamo operation. Given the robustness of the buoyant motions illustrated by our simulations, it seems that such a dynamo, powered solely by shear and hydromagnetic instabilities, should be a vital component of the physical processes governing the structure and evolution of accretion disks. Moreover, its operational range would extend into convectively stable regions of the disks, where field generation mechanisms that rely on an underlying turbulence cannot be applied. In a convectively stable region, the amplification of the seed field would not be hampered by the nonlinear effects discussed by Kulsrud & Anderson (1992) and Vainshtein & Cattaneo (1992), since the turbulence would appear only *after* a strong azimuthal field has been generated.

In an idealized scenario, the dynamo would be activated whenever a radial seed field appeared in the disk. The primary energy (the orbital energy of the disk gas) would be transformed into the azimuthal field energy, making the seed increasingly buoyant. The buoyancy effect in turn would transform the azimuthal field energy into kinetic energy of radial and vertical motions of the disk gas. These motions alone, without the help of the Coriolis effect, would be able to turn their own energy partly into the energy of the poloidal field through the kneading phenomenon discussed in § 3.4. At the same time, the vertical motions combined with the Coriolis effect would regenerate and/or amplify the initial seed. Dissipation of kinetic and magnetic energies within the disk would generate heat, resulting in an enhancement of buoyant motions by radiative energy inflow into the rising elements (see § 3.2 and Stella & Rosner 1984). Because of the MRI, the whole dynamo process would be necessarily accompanied by angular momentum transfer from lower to higher orbits and by an accretion flow. Thus, the expansion of an initially localized dynamo process would ensue, which could only be stopped in the regions where coupling between the field and the disk gas is inefficient owing to a very low degree of ionization.

However, many questions have to be answered before the above-outlined scenario could be adopted. Probably the most important one among them concerns the long-term evolution of the buoyant dynamo over periods comparable to, or longer than, the accretion timescale. One may suspect that the same buoyancy that is responsible for magnetization of the disk will slowly remove the field from the vicinity of the equatorial plane and drive the magnetized area toward the surface, eventually leading to complete *demagnetization* of the disk gas. A counterargument is that buoyancy does not operate at $z = 0$, and thus the removal of the magnetic field from the equatorial plane would not occur. Extensive numerical research is required to determine whether a strong equilibrium field can be maintained in the long term. Further, three-dimensional effects may not only support the dynamo action but also counteract it. For example, BGH find that weak azimuthal fields are also prone to the MRI. Thus, a suspicion arises that the buildup phase could be substantially shortened, saturating the dynamo at a much lower field intensity than suggested above. On the other hand, BGH point out that as time advances the wavelength of the dominant azimuthal mode of the MRI becomes longer. This would mean that the field is able to organize itself into more coherent structures which may eventually evolve into nearly axisymmetric patches. Another three-dimensional effect whose influence on the efficiency of the buoyant dynamo remains unclear is the undulating mode of the Parker instability, as a result of which the azimuthal field lines bend vertically. Again, extensive numerical research is needed to elucidate these issues. Finally, one may ask how the buoyant dynamo would operate in the presence of a turbulent velocity field *not related* to magnetic buoyancy (e.g., excited by thermal convection), and how it would react to an externally connected field threading the disk. While the answer to the latter qestion may be connected to the BGH results that indicate enhanced magnetoturbulence caused by the MRI, the interaction between convective flows and magnetic buoyancy effects seems to be too difficult a problem to be tackled at the present state of research.

We wish to thank K. R. Bell for providing vertical structure models for the initial disk. This work was performed under the auspices of a special NASA theory program which supports a joint Center for Star Formation Studies at NASA-Ames Research Center, University of California,

Berkeley, and University of California, Santa Cruz. Further support was provided by National Science Foundation grant AST-9315578 and by grant NAGW-3408 from the NASA Origins of Solar Systems Program. The calculations reported in the present paper were performed on the Cray EL-98 at the Interdisciplinary Center for Mathematical and Computational Modeling in Warsaw, Poland. M. R. acknowledges the support of the Committee for Scientific Research through the grant 2P 304 017 07. The MHD code was developed and tested while M. R. was a guest of the Princeton University Observatory. His visit to Princeton was supported by the grant AST-9313620.

REFERENCES

Alexander, D. 1975, ApJS, 29, 363
Bell, K. R., & Lin, D. N. C. 1994, ApJ, 427, 987
Bodenheimer, P., Yorke, H. W., Różyczka, M., & Tohline, J. E. 1990, ApJ, 355, 651
Brecher, A. 1972, in Origin of the Solar System, ed. H. Reeves (Paris: CNRS), 260
Butler, R. F. 1972, Earth Planet. Sci. Lett., 17, 120
Evans, C., & Hawley, J. F. 1988, ApJ, 332, 659
Galeyev, A. A., Rosner, R., & Vaiana, G. S. 1979, ApJ, 229, 318
Goodman, J., & Xu, G. 1994, ApJ, 432, 213
Hawley, J. F., & Balbus, S. A. 1991, ApJ, 376, 223
———. 1992, ApJ, 400, 595
Hawley, J. F., Gammie, C. F., & Balbus, S. A. 1995, ApJ, 440, 742
Kley, W., Papaloizou, J., & Lin, D. N. C. 1993, ApJ, 416, 679
Kulsrud, R. M., & Anderson, S. W. 1992, ApJ, 396, 606
Larson, R. 1984, MNRAS, 206, 197
Laughlin, G., & Bodenheimer, P. 1994, ApJ, 436, 335
Lin, D. N. C., & Papaloizou, J. 1980, MNRAS, 191, 37
Lubow, S. H., Papaloizou, J. C. B., & Pringle, J. E. 1994, MNRAS, 267, 235
Meyer, F., & Meyer-Hofmeister, E. 1983, A&A, 128, 420
Paczyński, B. 1978, Acta Astron., 28, 91
Parker, E. N. 1971, ApJ, 168, 239
———. 1975, ApJ, 198, 205
———. 1979, Cosmical Magnetic Fields (Oxford: Oxford Univ. Press)
———. 1992, ApJ, 401, 137
Pollack, J. B., McKay, C., & Christofferson, B. 1985, Icarus, 64, 471
Różyczka, M. 1985, A&A, 143, 59
Różyczka, M., Bodenheimer, P., & Bell, K. R. 1994, ApJ, 423, 736
Różyczka, M., Turner, N. J., & Bodenheimer, P. 1995, MNRAS, in press
Ruden, S. P., & Pollack, J. B. 1991, ApJ, 375, 740
Shakura, N. I., & Sunyaev, R. A. 1973, A&A, 24, 337
Shu, F., Najita, J., Ostriker, E., Wilkin, F., Ruden, S., & Lizano, S. 1994, ApJ, 429, 781
Stella, L., & Rosner, R. 1984, ApJ, 277, 312
Stepinski, T. F., Reyes-Ruiz, M., & Vanhala, H. A. T. 1993, Icarus, 106, 77
Stone, J. M., & Norman, M. L. 1992, ApJS, 80, 791
Tassoul, J.-L. 1978, Theory of Rotating Stars (Princeton: Princeton Univ. Press)
Tout, C. A., & Pringle, J. E. 1992, MNRAS, 259, 604
———. 1995, MNRAS, 272, 528
Vainshtein, S. I., & Cattaneo, F. 1992, ApJ, 393, 165